

Linear stability analysis and dynamic simulations of free convection in a differentially heated cavity in the presence of a horizontal magnetic field and a uniform heat source

Nikos A. Pelekasis^{a)}

Department of Mechanical and Industrial Engineering, University of Thessaly, Volos 38334, Greece

(Received 20 August 2005; accepted 31 January 2006; published online 23 March 2006)

The steady state and stability of two-dimensional free convection flow in a square cavity is examined, in the presence of a uniform internal heat source and a uniform magnetic field that is perpendicular to gravity and parallel to an imposed temperature gradient. The finite element method is used for calculating the steady and dynamic state of the system in the parameter space defined by the dimensionless numbers, Gr, Ha, Pr, and S. The trapezoidal rule is used for time integration. Linear stability analysis is performed by solving a generalized eigenvalue problem. The Arnoldi method is used for the calculation of eigenvalues with significant savings in storage and CPU time requirements. The base solution normally exhibits two recirculation regions when the heat production term is large enough. Stability analysis predicts a Hopf bifurcation to a periodic branch. A neutral stability diagram is constructed for a range of values of Ha, Gr, and S for liquid lithium, Pr=0.0321. Internal heat generation, i.e., increasing S, enhances instability by decreasing the critical value of Grashof, Gr_{cr} , determining the onset of the Hopf branch, whereas intensifying the magnetic field, i.e., increasing Ha, stabilizes the flow by increasing Gr_{cr} . Dynamic simulations confirm the above structure, identify the oscillatory solution branch as a supercritical Hopf bifurcation for the entire parameter range that was examined, and recover the time constants predicted by stability analysis. As Gr increases or as Ha decreases symmetric arrangement of the two rolls is eliminated and the steady flow configuration loses stability when $Gr > Gr_{cr}$. Subsequently, time periodicity sets in leading to more or less efficient heat removal in terms of lowering or increasing the average cavity temperature, in comparison with the steady flow configuration for the same Gr, depending on whether Ha lies below or above a critical value, respectively, for fixed S and Pr. © 2006 American Institute of Physics. [DOI: 10.1063/1.2185708]

I. INTRODUCTION

The coexistence of electromagnetic, hydrodynamic, and gravitational forces arises in a wide variety of flow arrangements that bear significance on a number of natural, e.g., the dynamic correlation between the magnetic field of earth and flow conditions in its core,¹ and technical applications, e.g., the design of thermal equipment for efficient cooling and regeneration of tritium from liquid lithium in plasma reactors of the tokamak type² and the manufacturing of high purity semiconductor crystals via the floating zone method.³ In the latter case, application of electric field stabilizes a capillary bridge of molten crystal, which can thus acquire a uniform cylindrical shape while maintaining a length to radius ratio that is significantly larger than unity. Stability analysis performed numerically using the finite element method and subsequent eigenvalue calculations provide the parameter range over which the base cylindrical configuration remains stable against axisymmetric disturbances and quantify the beneficial effect of the electric field on the stability of the interface that is formed between the crystal and the surrounding medium when both are treated as leaky dielectrics.⁴

In the context of tokamak reactor design it is of interest

to coordinate the processes of heat removal and tritium regeneration that take place in specially designed modules occupying the blanket of the reactor. According to some of the design alternatives that are investigated, breeding of tritium and cooling of the reactor are carried out in different compartments of the blanket. In the modules where heat removal is of primary interest liquid metal, e.g., liquid lithium, is pumped through the use of a high-pressure head that is necessary for high heat transfer rates to be achieved. In regions where liquid metal breeding takes place liquid lithium is slowly pumped, acting as the operating medium, and absorbs radiation in the form of neutrons emitted inside the core of the reactor, in order to provide the tritium needed for the fusion reaction that takes place inside the core to be sustained.⁵ This entails a highly exothermal reaction and, consequently, proper removal of the large amount of heat that is generated in the blanket is an additional design parameter that needs to be considered. This is a flow situation where free convection dominates over forced convection while an interesting interplay of different forces is observed that determines the dynamic behavior of the system and will affect the final design of the reactor. Most notably the effect of the Lorenz force, generated as a result of the interaction between the strong toroidal magnetic field of tokamak reac-

^{a)}Telephone: 30-24210-74102. Fax: 30-24210-74050. Electronic mail: pel@uth.gr

tors and the electric current motion in the blanket, on the flow stability should be investigated.

The stability of forced convection in rectangular ducts has been investigated both experimentally and theoretically/numerically. In particular, it is known from experimental investigations,⁶ with liquid metal flows through rectangular ducts subjected to an intense transverse magnetic field, that laminar fully developed flow becomes unstable due to three-dimensional convection. In this parameter range it is also known that, adjacent to the two duct walls that are parallel to the magnetic field, two layers are formed with thickness in the order of $Ha^{-1/2}$ where the fluid velocity is much larger than any other part of the cross section; Ha denotes the Hartmann number that serves as a measure of the intensity of the magnetic forces. These layers are called “side layers” and also appear in the case of free convection. In the same parameter range of large Hartmann numbers, two layers with thickness in the order of Ha^{-1} are formed adjacent to the two walls that are perpendicular to the magnetic field. These layers are called “Hartmann layers” and appear in the case of free convection as well. Ting *et al.*⁷ attribute the destabilization of fully developed duct flow to the large velocities prevailing in the “side layers.” In this context, they performed stability analysis on the flow configuration pertaining to the side boundary layers and obtained a critical value of Re for the onset of convection that is well below the experimentally observed value. Nevertheless, their analysis is in qualitative agreement with experimental findings of two-dimensional vortices that are aligned with the magnetic field and are confined within the side walls, for forced convection in ducts.⁸ On the other hand, Lingwood and Alboussière⁹ examined the stability of the Hartmann boundary layer in the limit of infinitesimal disturbances and they identified a critical value for Re/Ha for stability that is well above the experimentally observed value for transition. By resorting to an energy approach that accounts for finite disturbances they were able to find a more reasonable threshold value $abcd$ for Re/Ha . This finding is corroborated by weakly nonlinear analysis¹⁰ where subcritical destabilization of the base solution corresponding to the Hartmann layer is verified for values of Re/Ha that are below the critical.

In the case of buoyant magnetohydrodynamic flow in ducts formation of the above-mentioned side and Hartmann layers is also observed along with a core flow, which may be of three-dimensional nature.¹¹ In the same study the effect of wall electric conductivity was identified for the first time. In fact it was pointed out that for perfectly conducting walls high velocity jets are formed near the sidewalls which carry most of the flow. This result has important implications in the amount of heat that is being transferred, provided that this structure remains stable. The formation of a quasi-two-dimensional convective roll pattern that is aligned with the magnetic field is captured experimentally and theoretically via linear stability analysis,¹² with the critical value of the Rayleigh number, Ra , increasing roughly like Ha^2 as Ha increases. In that study, the magnetic field is allowed to vary and is positioned perpendicularly with respect to the temperature gradient and the direction of gravity. As a result of this arrangement Joule dissipation destroys vortices that are

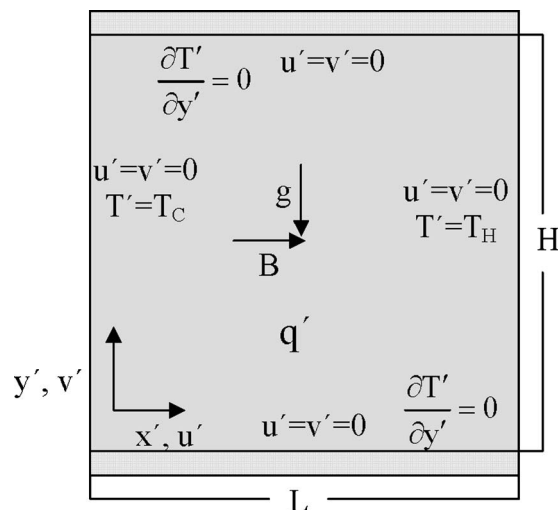


FIG. 1. Schematic diagram of the flow arrangement.

perpendicular to the magnetic field while elongating the ones parallel to it. The stabilizing effect of the magnetic field was also obtained¹³ for the case of buoyant flow between two vertical plates held at constant temperature difference with a uniform external magnetic field that is perpendicular to gravity. Transition from stationary to traveling waves in the direction perpendicular to the two plates was also obtained indicating the feasibility of periodic solutions when a bounded domain is considered. Finally, numerical simulations of internally heated buoyant flow in rectangular and cubic enclosures, were performed by Arcidiacono *et al.* in the absence of a magnetic field¹⁴ and by Ciofalo and Cricchio for magnetohydrodynamic flows,¹⁵ respectively. In the former study the effect of Grashof number, $Gr = Ra/Pr$, on the transition from symmetric to asymmetric solutions and then from steady to periodic and chaotic solutions was investigated numerically. In the latter reference the effects of the magnetic field and three-dimensionality are included and the appearance of side and Hartmann layers as Ha increases are verified.

In the present study the case of two-dimensional natural convection in a rectangular cavity is investigated, in the presence of a uniform magnetic field that is perpendicular to gravity and aligned to the constant temperature gradient imposed upon the two vertical sides, Fig. 1. This particular arrangement of the magnetic field is believed¹⁵ to better suppress instabilities, as verified by the results to be presented in the following sections. The cavity is uniformly heated and liquid lithium is taken to be the operating fluid in order to better simulate flow conditions in liquid metal breeders. Nevertheless, similar flow configurations are pertinent to crystal growth processes.¹⁶ As a first step, three-dimensional convection is not accounted for. Rather, the steady state and stability of two-dimensional solutions is examined, focusing on the effect of Ha and Gr on symmetry and stability and, subsequently, on the efficiency of heat removal. However, the flow pattern obtained here contains the necessary structure, i.e., core flow, Hartmann and side layers, in order to provide the base flow for a stability analysis that will allow

for three-dimensional disturbances that are periodic in the spanwise direction. The latter direction is aligned with the vorticity vector of the two-dimensional solutions obtained in the present study, and it will be very interesting to examine how vortices that evolve in this direction, such as those observed elsewhere,¹² arise as bifurcations of two-dimensional solutions that account for wall effects, such as those presented in the following sections. This investigation can be carried out with the numerical methodology employed here and will be presented in a future study.

The detailed problem formulation is given in Sec. II. In Sec. III the formulation for stability analysis is outlined, on two-dimensional steady state solutions. Steady state solutions, which are inherently asymmetric due to the temperature gradient, are obtained numerically and their stability can also be examined via dynamic simulations of the full 2D problem. Numerical solution entails application of the finite element method along with a time integration scheme, as described in Sec. IV. In the same section, the methodology for numerical evaluation of eigenvalues is presented, by solving a generalized eigenvalue problem via the Arnoldi method.¹⁷ The Arnoldi method utilizes the banded structure of the Jacobian matrix produced by the finite element solution of the nonlinear governing equations and affords calculation of the most important eigenvalues, thus allowing for consideration of the numerically obtained 2D steady state as the base solution as opposed to an asymptotic result. In Sec. V the asymptotic solution is obtained in the limit of negligible inertia in comparison with magnetic forces, and is compared against numerical results. Then, in Sec. VI, a complete neutral stability diagram is constructed in the parameter space defined by Gr , Ha , and the dimensionless heat production, S , demonstrating the range of validity of steady state solutions. The results of steady and dynamic simulations are presented in Secs. VI B and VI C. Bifurcation diagrams are constructed numerically, illustrating the evolution of a characteristic property of the solution, such as the difference in the amount of heat that is removed from the cavity through the two vertical sides, with varying parameter values. Periodic branches are captured and their effect on the solution is illustrated on the bifurcation diagram. Finally, in Sec. VII conclusions are drawn and directions for future research are pointed out.

II. PROBLEM FORMULATION

We consider two-dimensional free convection in a square cavity where a uniform external magnetic field is applied perpendicularly to the direction of gravity and the Boussinesq condition holds, $\beta(T_h - T_c) \ll 1$. $T_h - T_c$ is the temperature gradient that is established between the right and left vertical sides of the cavity, Fig. 1, and β the coefficient of thermal expansion of the liquid that fills the cavity:

$$\rho = \rho_0[1 - \beta(T - T_{Av})], \quad T_{Av} = (T_c + T_h)/2. \quad (1)$$

Since in most of the applications where this flow arrangement applies liquid melts of lithium alloys (e.g., Pb-17Li) are used as operating fluids, in the following we will use the thermophysical properties of lithium in order to set up the

dimensionless variables that are involved in the problem formulation, $Pr = \nu/\alpha = 0.0321$, where α and ν denote the thermal diffusivity and kinematic viscosity of liquid lithium, respectively. For this type of operating fluid the magnetic Reynolds number, $Re_m = \sigma\mu_0\nu$ with $(\sigma\mu_0)^{-1}$ denoting the magnetic diffusivity of lithium, is a very small quantity and consequently magnetic induction is negligible and the magnetic field is uniform everywhere in the cavity, $\mathbf{B}' = \mathbf{B}_0 = B_0\mathbf{e}_x$. The current density is obtained via Ohm's law,

$$\mathbf{j}' = -\nabla\phi' + \mathbf{v}' \times \mathbf{B}', \quad (2)$$

where ϕ' is the electric potential and \mathbf{v}' the velocity vector, which in conjunction with the requirement for continuity of the electric charge,

$$\nabla \cdot \mathbf{j}' = 0, \quad (3)$$

gives,

$$\nabla^2\phi' = \boldsymbol{\omega}' \cdot \mathbf{B}'; \quad (4)$$

throughout this study primed quantities denote dimensional variables. At this point it should be stressed that we take the characteristic length in the third spatial direction to be much larger than the length of the sides of the cavity and consequently we ignore variations in the spanwise direction. Thus, the velocity field is effectively two-dimensional, except for the two edges of the long spanwise direction where three-dimensional effects should be accounted for. Then the vorticity vector is perpendicular to the plane of the cavity where the magnetic field lies and the electric potential satisfies the Laplacian. However, due to the negligible three-dimensional effects in the main section of the spanwise direction, variations in the electric potential can also be ignored in this region and consequently we set

$$\mathbf{j}' = \mathbf{v}' \times \mathbf{B}'. \quad (5)$$

Thus, the only nonzero component of current density \mathbf{j}' points towards the positive and negative spanwise direction depending on the sign of the transverse component of velocity. It does not vary in that direction except for a narrow region adjacent to the two ends of the duct that is formed as the studied cross section is projected along the spanwise direction, where the other two components of current density are also needed in order to close the path of the electric current.

Choosing the length L of each one of the cavity sides as the characteristic length, the temperature gradient ΔT as the characteristic temperature and the balance between gravitational and inertial forces in order to render time, velocity, and pressure dimensionless, we obtain:

$$t' = \frac{t'}{\sqrt{L/(g\beta\Delta T)}}, \quad \mathbf{x}' = \frac{\mathbf{x}'}{L}, \quad P' = \frac{P' = p' + \rho_0gy}{\rho g\beta\Delta TL}, \quad (6)$$

$$\mathbf{u}' = \frac{\mathbf{u}'}{\sqrt{g\beta\Delta TL}}, \quad T = \frac{T' - T_{Av}}{T_h - T_{Av}}, \quad \mathbf{B}' = \frac{\mathbf{B}'}{B_0}.$$

In this fashion the dimensionless formulation of the entire problem reads: continuity

$$\nabla \cdot \mathbf{u} = 0, \quad (7)$$

x momentum

$$\frac{\partial u}{\partial t} + u \frac{\partial u}{\partial x} + v \frac{\partial u}{\partial y} = -\frac{\partial P}{\partial x} + \text{Gr}^{-1/2} \left(\frac{\partial^2 u}{\partial x^2} + \frac{\partial^2 u}{\partial y^2} \right), \quad (8)$$

y momentum

$$\begin{aligned} \frac{\partial v}{\partial t} + u \frac{\partial v}{\partial x} + v \frac{\partial v}{\partial y} = & -\frac{\partial P}{\partial y} + \text{Gr}^{-1/2} \left(\frac{\partial^2 v}{\partial x^2} + \frac{\partial^2 v}{\partial y^2} \right) + T \\ & - \frac{\text{Ha}^2}{\text{Gr}_E^{1/2}} v, \end{aligned} \quad (9)$$

energy balance

$$\frac{\partial T}{\partial t} + u \frac{\partial T}{\partial x} + v \frac{\partial T}{\partial y} = \frac{1}{\text{Gr}^{1/2} \text{Pr}} \nabla^2 T + \frac{S}{\text{Gr}^{1/2}} \quad (10)$$

with boundary conditions

$$T(x=0, y) = -1 \quad T(x=1, y) = 1 \quad (11)$$

$$\frac{\partial T}{\partial y}(x, y=0) = \frac{\partial T}{\partial y}(x, y=1) = 0$$

$$u(x=0, y) = v(x=0, y) = 0, \quad u(x=1, y) = v(x=1, y) = 0, \quad (12a)$$

$$u(x, y=0) = v(x, y=0) = 0, \quad u(x, y=A) = v(x, y=A) = 0. \quad (12b)$$

The following dimensionless parameters are involved in the formulation:

$$\text{Gr} = \frac{g\beta\Delta TL^3}{\nu^2}, \quad \text{Ha} = \sqrt{\frac{L^2 \sigma B_0^2}{\rho\nu}}, \quad S = \frac{qL^2}{\Delta T \rho c_p \nu}, \quad (13)$$

$$\text{Pr} = \frac{\nu}{\alpha}, \quad A = \frac{H}{L} = 1,$$

where A is the aspect ratio of the cavity set to one in the present study and Gr , Ha , S signify the relative importance of gravitational and viscous forces, magnetic and viscous forces, and the dimensionless heat production, respectively. In Eq. (9) the term involving the dimensionless temperature represents buoyancy, whereas the last term on the right-hand side of the same equation represents the Lorenz force,

$$\mathbf{j} \times \mathbf{B} = (\mathbf{v} \times \mathbf{B}) \times \mathbf{B} = -\nu \mathbf{e}_y. \quad (14)$$

The production term in Eq. (10) signifies the amount of heat that is being released when a volumetric heat source is present as is the case, for example, when liquid lithium is used for breeding tritium via a highly exothermal reaction; q is the dimensional volumetric rate of heat production in the duct. Equations (7)–(12) can be solved to provide the dynamic state of the system when three-dimensional effects are neglected. When the time dependent terms in Eqs. (8)–(10) are dropped, steady state solutions are obtained.

In an effort to quantify and monitor the effect of symmetry on the steady state and stability of the problem, the

average dimensionless Nusselt number was defined on each one of the two vertical sides, along with the average dimensionless cavity temperature. If we integrate the energy conservation equation over the cavity area and we incorporate the boundary conditions of zero velocity at the walls and zero heat flux at the top and bottom walls, we obtain:

$$\begin{aligned} - \int_L \frac{\partial T}{\partial n_L} ds - \int_R \frac{\partial T}{\partial n_R} ds = & \int_L \frac{\partial T}{\partial x} dy + (-1) \int_R \frac{\partial T}{\partial x} dy \\ = & \text{Nu}_L + \text{Nu}_R = \text{Pr} S, \end{aligned} \quad (15)$$

where L and R denote the left and right vertical sides of the cavity, $\mathbf{n}_L = -\mathbf{e}_x$ and $\mathbf{n}_R = \mathbf{e}_x$ the outwards pointing normal vectors corresponding to the same two sides, respectively, and Nu_L and Nu_R the amount of heat being removed through each one of the two sides. Clearly, for a steady state solution the total amount of heat removed from the cavity should be equal to the amount produced internally, as indicated by Eq. (15). The latter also serves as an integral check of accuracy of our calculations. The difference between the two Nusselt numbers can be used as a bifurcation parameter of our parametric study that measures the departure from symmetry of a certain steady state solution. Alternatively, and since we are ultimately interested in estimating the efficiency of heat removal from the cavity in the parameter range of relevance to our problem, the average temperature of the cavity can be used as the bifurcation parameter:

$$T_{\text{AV}} = \int_0^1 dx \int_0^1 dy T(x, y), \quad (16a)$$

$$\langle T_{\text{AV}} \rangle = \frac{\int_0^{t_0} dt \int_0^1 dx \int_0^1 dy T(x, y, t)}{t_0}. \quad (16b)$$

The second parameter, $\langle T_{\text{AV}} \rangle$, is useful in identifying the dynamic behavior of periodic solutions with period T_0 , hence the additional averaging over one period of oscillations.

III. STABILITY ANALYSIS

As will be seen in the following sections the main steady state branch that is obtained is the one that evolves from the zero Gr solution via simple continuation in the parameter (Gr , Ha , S) space. We want to evaluate the stability of this branch with respect to two-dimensional disturbances that lead to bifurcations that represent, either steady state branches of different nature as far as symmetry is concerned or periodic solutions. Subsequently, we want to investigate the effect of this dynamic behavior on the overall cooling of the cavity when heat sources are present. To this end, we introduce infinitesimally small disturbances for all the dependent variables,

$$\begin{bmatrix} \mathbf{u}(x, y, t) \\ P(x, y, t) \\ T(x, y, t) \end{bmatrix} = \begin{bmatrix} \mathbf{u}_0(x, y) \\ P_0(x, y) \\ T_0(x, y) \end{bmatrix} + \varepsilon \begin{bmatrix} \mathbf{u}_1(x, y) \\ P_1(x, y) \\ T_1(x, y) \end{bmatrix} e^{\sigma t} + O(\varepsilon^2), \quad (17)$$

where 0 and 1 as indices denote the steady state and disturbed states, respectively, ε is a measure of the amplitude of

the initial disturbance that is taken to be negligibly small, $\varepsilon \ll 1$, for the purpose of stability analysis and σ is the eigenvalue that determines the asymptotic behavior of the system as time $t \rightarrow \infty$. The steady state solution is asymptotically unstable if an eigenvalue exists whose real part, σ_r , is positive. If no such eigenvalue exists then the steady state solution is stable for the corresponding set of parameter values.¹⁸ As the problem parameters vary, Gr, Ha or S, so do the eigenvalues until a point is reached for which σ_r crosses zero in which case we have neutral stability and a bifurcating solution arises. Depending on the imaginary part, σ_i , if it vanishes, a new steady state solution emerges, whereas if it is nonzero, then a Hopf bifurcation exists that leads to a periodic branch.

Upon substitution of Eq. (17) in the governing equation of the problem, Eqs. (7)–(10), and dropping terms that are $O(\varepsilon^2)$ or smaller we obtain the following stability problem,

$$\frac{\partial u_1}{\partial x} + \frac{\partial v_1}{\partial y} = 0, \quad (18)$$

$$\begin{aligned} \sigma u_1 + \frac{\partial(u_0 u_1)}{\partial x} + v_0 \frac{\partial u_1}{\partial y} + v_1 \frac{\partial u_0}{\partial y} \\ = -\frac{\partial P_1}{\partial x} + \text{Gr}^{-1/2} \left(\frac{\partial^2 u_1}{\partial x^2} + \frac{\partial^2 u_1}{\partial y^2} \right), \end{aligned} \quad (19)$$

$$\begin{aligned} \sigma v_1 + \frac{\partial(v_0 v_1)}{\partial y} + u_0 \frac{\partial v_1}{\partial x} + u_1 \frac{\partial v_0}{\partial x} \\ = -\frac{\partial P_1}{\partial y} + \text{Gr}^{-1/2} \left(\frac{\partial^2 v_1}{\partial x^2} + \frac{\partial^2 v_1}{\partial y^2} \right) + T_1 - \frac{\text{Ha}^2}{\text{Gr}^{1/2}} v_1, \end{aligned} \quad (20)$$

$$\sigma T_1 + u_1 \frac{\partial T_0}{\partial x} + u_0 \frac{\partial T_1}{\partial x} + v_0 \frac{\partial T_1}{\partial y} + v_1 \frac{\partial T_0}{\partial y} = \frac{\text{Gr}^{-1/2}}{\text{Pr}} \nabla^2 T_1 \quad (21)$$

along with the homogeneous part of boundary conditions (11) and (12). The above equations constitute an eigenvalue problem for σ , which can be discretized to provide the eigenvalues and eigenvectors, u_1, v_1, P_1, T_1 , corresponding to the basic steady state solution. The eigenvectors are very important as they contain the essential features of the bifurcating solution, and can be utilized for obtaining a reliable initial guess for numerical evaluation of a solution vector of the new branch in the vicinity of the bifurcation point.¹⁹

IV. NUMERICAL METHODOLOGY

Numerical discretization of Eqs. (7)–(12) for calculating the steady or the dynamic state of the problem, and of Eqs. (18)–(21) for the eigenvalues and eigenvectors related to a specific basic solution, is carried out via the finite element method.⁴ The x and y components of the velocity vector, the temperature and the pressure of liquid lithium are represented by biquadratic Lagrangian basis functions, $\Phi_i(x, y)$, and bilinear Lagrangian basis functions, $\Psi_i(x, y)$, respectively,

$$\begin{bmatrix} u \\ v \\ T \end{bmatrix} (x, y) = \sum_{i=1}^N \begin{bmatrix} u_i \\ v_i \\ T_i \end{bmatrix} \Phi_i(x, y), \quad P(x, y) = \sum_{i=1}^M p_i \Psi_i(x, y), \quad (22)$$

where u_i, v_i, T_i, p_i , are the coefficients of the Lagrangian representations, which are identical with the values of the corresponding dependent variables at the interpolation nodes and N, M represent the number of coefficients in each summation. Galerkin's procedure is employed in order to construct the residual equations. Equation (7) is multiplied by trial function $\Psi_i(x, y)$, Eqs. (8)–(10) by trial function $\Phi_i(x, y)$, and subsequently they are integrated over the area of the cavity. On applying the divergence theorem second order derivatives are eliminated from Eqs. (8)–(10) and the weak formulation is obtained:

$$\oint \Psi_i \left(\frac{\partial u}{\partial x} + \frac{\partial v}{\partial y} \right) dx dy = 0, \quad i = 1, M, \quad (23)$$

$$\begin{aligned} \sum_{j=1}^N \left(\oint \Phi_i \Phi_j dx dy \right) \frac{du_j}{dt} + \oint \left[\Phi_i \left(u \frac{\partial u}{\partial x} + v \frac{\partial u}{\partial y} \right) - P \frac{\partial \Phi_i}{\partial x} \right. \\ \left. + \text{Gr}^{-1/2} \left(2 \frac{\partial u}{\partial x} \frac{\partial \Phi_i}{\partial x} + \frac{\partial \Phi_i}{\partial y} \left(\frac{\partial u}{\partial y} + \frac{\partial v}{\partial x} \right) \right) \right] dx dy \\ - \oint \Phi_i \left[-P n_x + \text{Gr}^{-1/2} \left(2 \frac{\partial u}{\partial x} n_x + \left(\frac{\partial u}{\partial x} + \frac{\partial v}{\partial y} \right) n_y \right) \right] ds = 0, \quad i = 1, N, \end{aligned} \quad (24)$$

$$\begin{aligned} \sum_{j=1}^N \left(\oint \Phi_i \Phi_j dx dy \right) \frac{dv_j}{dt} + \oint \left[\Phi_i \left(u \frac{\partial v}{\partial x} + v \frac{\partial v}{\partial y} \right) - P \frac{\partial \Phi_i}{\partial y} \right. \\ \left. + \text{Gr}^{-1/2} \left(2 \frac{\partial v}{\partial y} \frac{\partial \Phi_i}{\partial y} + \frac{\partial \Phi_i}{\partial x} \left(\frac{\partial u}{\partial y} + \frac{\partial v}{\partial x} \right) \right) \right] dx dy \\ + \oint \left(\frac{\text{Ha}^2}{\text{Gr}^{1/2}} v - T \right) \Phi_i dx dy - \oint \Phi_i \left[-P n_y \right. \\ \left. + \text{Gr}^{-1/2} \left(2 \frac{\partial v}{\partial y} n_y + \left(\frac{\partial u}{\partial y} + \frac{\partial v}{\partial x} \right) n_x \right) \right] ds = 0, \quad i = 1, N, \end{aligned} \quad (25)$$

$$\begin{aligned} \sum_{j=1}^N \left(\oint \Phi_i \Phi_j dx dy \right) \frac{dT_j}{dt} + \oint \left[\Phi_i \left(u \frac{\partial T}{\partial x} + v \frac{\partial T}{\partial y} \right) \right. \\ \left. + \frac{\text{Gr}^{-1/2}}{\text{Pr}} \left(\frac{\partial \Phi_i}{\partial x} \frac{\partial T}{\partial x} + \frac{\partial \Phi_i}{\partial y} \frac{\partial T}{\partial y} \right) - \Phi_i \text{Gr}^{-1/2} S \right] dx dy \\ - \oint \Phi_i \left(\frac{\partial T}{\partial x} n_x + \frac{\partial u}{\partial y} n_y \right) ds = 0, \quad i = 1, N. \end{aligned} \quad (26)$$

In the above equations ds denotes the differential arc length along the perimeter of the cavity, whereas the line integrals appear due to the divergence theorem. Terms inside square brackets in the line integrals of Eqs. (24) and (25) correspond to the x and y components of the force exerted on the cavity

boundaries, $(-P\bar{\mathbf{T}} + \bar{\boldsymbol{\tau}}) \cdot \mathbf{n}$, where $\bar{\mathbf{T}}$ and $\bar{\boldsymbol{\tau}}$ denote the unity and the deviatoric stress tensors and \mathbf{n} the unit normal on the sides of the cavity. It should be stressed that due to the essential boundary conditions that are applied on the cavity sides for the two velocity components and the essential and no flux conditions applied for the temperature field, the line integrals in Eqs. (24)–(26) will not affect the numerical solution of the problem.²⁰

When steady state solutions are sought, the time derivatives of the coefficients are set to zero and the problem formulation assumes the form,

$$R_{Ci}(c_j) = 0, \quad i = 1, M, \quad R_{Mxi}(c_j) = R_{Mxi}(c_j) = R_{Txi}(c_j) = 0, \quad (27a)$$

$$i = 1, N,$$

$$c = [(p_k), (u_l), (v_l), (T_l)], \quad R = [(R_{Ck}), (R_{Mxi}), (R_{Myi}), (R_{Tl})], \quad (27b)$$

$$k = 1, M \quad l = 1, N,$$

where R_{Ci} , R_{Mxi} , R_{Myi} , R_{Ti} , denote the residuals that arise from Eqs. (23)–(26) after the transient terms are dropped. Numerical evaluation of the unknown coefficients c_i of the finite element representation of the dependent variables is carried out via the Newton-Raphson iterative scheme in the following fashion:

$$J_{ij}(c_i^k) \Delta c_j = R_i(c_i^k), \quad \Delta c_i = c_i^k - c_i^{k+1}, \quad J_{ij}(c_i^k) = \frac{\partial R_i}{\partial c_j^k}(c_i^k), \quad (28)$$

where J_{ij} denotes the elements of the Jacobian matrix and k is the Newton's iterations index. Convergence is monitored via the Euclidian norm, $\sqrt{\sum_i \Delta c_i^2}$, of the incremental vector Δc_i between successive iterations.

Once convergence is ascertained and a steady state solution, c_{0i} , calculated its stability is investigated via the finite element solution of the eigenvalue problem (18)–(21). It should be noted that, owing to the linear nature of the stability problem, aside from the mass matrix that arises in the process of discretizing the transient terms involving eigenvalue σ on the left-hand side of (19)–(21), discretization of the rest of the terms in Eqs. (18)–(21) reproduces the Jacobian matrix corresponding to the converged solution, $J_{ij}(c_{0i})$. Consequently, the eigenvalues are provided by the generalized eigenvalue problem

$$J_{ij}^{-1}(c_{0i}) B_{jn} c_{1n} = \tau c_{1i}, \quad \tau = \frac{-1}{\sigma}, \quad (29)$$

where B_{ij} is the mass matrix and c_{1j} the eigenvector corresponding to eigenvalue σ . The eigenvector is very useful for providing a reliable initial guess, $c_{0i} + \epsilon c_{1i}$, in the process of obtaining a numerical solution on bifurcating branches in the vicinity of a bifurcation point.¹⁹ The latter is a point in the parameter space for which σ_τ crosses zero. Both the Jacobian and the mass matrices are banded and this alleviates the computational load required for numerical solution of the eigenvalue problem. In order to incorporate this feature in the eigenvalue calculation the Arnoldi method is employed that calculates the eigenvalues with the largest real part or abso-

lute value. Since we are mainly interested in the eigenvalues with vanishing real part, i.e., those signifying bifurcation points in the parameter space, we introduce the transformation

$$\sigma B_{ij} c_{1j} + J_{ij}(c_{0i}) c_{1j} = 0 \rightarrow J_{ij}(c_{0i}) c_{1j} = -\sigma B_{ij} c_{1j}. \quad (30)$$

Thus, the eigenvalues of the original problem with small magnitude are mapped onto those with large magnitude in the transformed problem. Other approaches exist in the literature,²¹ employing Cayley transforms that take into account the fact that the imaginary part of the eigenvalue is nonzero in a Hopf bifurcation. Nevertheless, the transform in Eq. (30) was seen to furnish accurate results for the Hopf bifurcations that arise in our case; hence we used it throughout the present study. It should be also stressed that the eigenvalues with the largest magnitude live in a Krylov subspace¹⁷ of the complete set of eigenvalues and can be calculated without knowing the complete set. To this end a small number of eigenvalues is calculated via the Arnoldi method. The number is increased until convergence of the largest eigenvalues is established and the process is stopped. The eigenvectors and eigenvalues are calculated via an iterative process that is initiated by a random initial guess, $c_{1i} = c_{1i}^0$. Subsequent corrections are found by

$$\tau_{k+1} = \|J_{ij}^{-1}(c_{0i}) B_{jn} c_{1n}^k\|, \quad c_{1i}^{k+1} = \frac{J_{ij}^{-1}(c_{0i}) B_{jn} c_{1n}^k}{\|J_{ij}^{-1}(c_{0i}) B_{jn} c_{1n}^k\|}, \quad (31)$$

when the eigenvectors are scaled so that $\|c_{1i}^k\| = 1$. The method converges to the largest eigenvalue, τ_1 , with a speed that is proportional to the ratio $|\tau_2|/|\tau_1|$, where τ_2 is the second largest eigenvalue. An important aspect of the approach is that the banded structure of the two matrices can be utilized. In addition, owing to the simple format and symmetry of mass matrix B_{ij} , the latter need not be fully constructed. Rather it is evaluated on an elemental basis concurrently with its multiplication with J_{ij} . This significantly reduces the storage requirements of the solution procedure. At the most, 300 eigenvalues were seen to be enough for capturing the system dynamics.

As a means to verify the bifurcation structure provided by stability analysis, but also to identify possible disjointed solution branches, two-dimensional dynamic simulations were carried out for the same parameter range. To this end, the time derivatives are retained in Eqs. (23)–(26) and the trapezoidal rule is employed for time discretization, due to its increased stability and accuracy characteristics. Consequently, the numerical formulation formally reads,

$$B_{ij} \frac{c_j^{k,n} - c_j^o}{\Delta t} = -\frac{R_i^{k,n}(c_i^{k,n}) + R_i^o(c_i^o)}{2}, \quad (32)$$

where B_{ij} , $c_i^{k,n}$, $R_i^{k,n}$ bear the connotation ascribed to them in the previous paragraphs and superscripts n and o denote the new and old time locations, respectively. Finally, the following problem is solved via the Newton-Raphson iterative procedure at every time instant:

$$\left[\frac{B_{ij}}{\Delta t} + \frac{J_{ij}(c_i^{k,n})}{2} \right] \Delta c_j^{k,n} = S_i^k, \quad \Delta c_j^{k,n} = c_j^{k,n} - c_j^{k+1,n}, \quad (33)$$

$$S_i^k = B_{ij} \frac{c_j^{k,n} - c_j^o}{\Delta t} + \frac{R_i^{k,n}(c_i^{k,n}) + R_i^o(c_i^o)}{2}.$$

Again, construction of only one banded system matrix is required.

Numerical accuracy of the entire method is estimated to be $O(\Delta t^2, \Delta x^2, \Delta y^2)$ for the velocity and temperature fields. The results presented in the following sections have been checked for convergence with a mesh consisting of 30×30 and 60×60 biquadratic Lagrangian elements. When boundary layers develop adjacent to the four sides of the cavity algebraic packing of the element size is applied in order to capture abrupt variations of the dependent variables in these regions. More specifically, near the walls a graded mesh was used with the dimensionless distance of the element edges from the nearest wall varying algebraically, e.g., when packing is applied on the x direction nodes,

$$x_1 = 0, \quad x_{2I} = \frac{x_{2I-1} + x_{2I+1}}{2}, \quad x_{2I+1} = \left(\frac{I}{N} \right)^{X_{\text{fact}}}, \quad (34a)$$

$$I = 2, 3, \dots, N/2,$$

$$x_{2N+1} = 1, \quad x_{2I} = \frac{x_{2I-1} + x_{2I+1}}{2}, \quad (34b)$$

$$x_{2I-1} = 1 - \left(\frac{N+1-I}{N} \right)^{X_{\text{fact}}}, \quad I = N, N-1, \dots, N/2+1,$$

where N is the total number of elements used in the x direction and X_{fact} is a number that is taken to be in the vicinity of, and always larger than 1.

The time step is controlled by the period of the bifurcating solution, determined by the imaginary part of the eigenvalue whose real part crosses zero in the stability analysis. In most of the simulations presented in the following sections a dimensionless time step of $\Delta t = 0.0025$ was used.

V. ASYMPTOTIC ANALYSIS IN THE LIMIT $\text{Gr}^{1/2}/\text{Ha}^2 \rightarrow 0$

The case of large Ha in comparison to Gr , signifying dominance of magnetic over inertia forces, is very important due to its relevance to flow arrangements that are often met in the blanket section of fusion reactors,¹² but also as a means to check the validity of our numerical methodology against asymptotic results. In this case rescaling of the governing equations is necessary so that the dominant balance between magnetic forces and buoyancy is reflected in the problem formulation. Thus velocity, time and pressure are rendered dimensionless as,

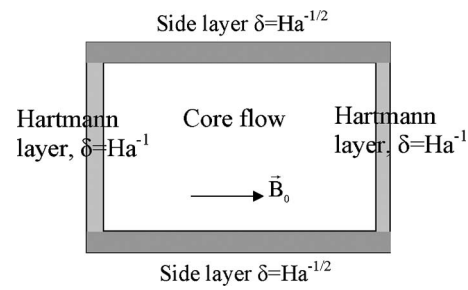


FIG. 2. Flow structure in the limit of large Ha .

$$\hat{\mathbf{u}} = \frac{\hat{\mathbf{u}}'}{\rho_0 \beta g \Delta T / (\sigma B_0^2)}, \quad \hat{t} = \frac{t'}{L \sigma B_0^2 / (\rho_0 \beta g \Delta T)}, \quad (35)$$

$$\hat{P} = \frac{P'}{\rho_0 \beta g \Delta T L}$$

and the governing equations of the problem become:

$$\frac{\text{Gr}}{\text{Ha}^4} \left(\frac{\partial \hat{u}}{\partial \hat{t}} + \hat{u} \frac{\partial \hat{u}}{\partial x} + \hat{v} \frac{\partial \hat{u}}{\partial y} \right) = - \frac{\partial \hat{P}}{\partial x} + \frac{1}{\text{Ha}^2} \left(\frac{\partial^2 \hat{u}}{\partial x^2} + \frac{\partial^2 \hat{u}}{\partial y^2} \right), \quad (36)$$

$$\frac{\text{Gr}}{\text{Ha}^4} \left(\frac{\partial \hat{v}}{\partial \hat{t}} + \hat{u} \frac{\partial \hat{v}}{\partial x} + \hat{v} \frac{\partial \hat{v}}{\partial y} \right) = - \frac{\partial \hat{P}}{\partial y} + \frac{1}{\text{Ha}^2} \left(\frac{\partial^2 \hat{v}}{\partial x^2} + \frac{\partial^2 \hat{v}}{\partial y^2} \right) + T - \hat{v}, \quad (37)$$

$$\frac{\text{Gr}^{1/2}}{\text{Ha}^2} \left(\frac{\partial T}{\partial \hat{t}} + \hat{u} \frac{\partial T}{\partial x} + \hat{v} \frac{\partial T}{\partial y} \right) = \frac{1}{\text{Gr}^{1/2} \text{Pr}} \nabla^2 T + \frac{S}{\text{Gr}^{1/2}}, \quad (38)$$

$$\frac{\partial \hat{u}}{\partial x} + \frac{\partial \hat{v}}{\partial x} = 0. \quad (39)$$

When $\text{Gr}^{1/2}/\text{Ha}^2 \rightarrow 0$ convective terms in the above equations are dropped leaving a linear problem of heat conduction in a cavity where heat sources are present. Heat production generates large temperature gradients in addition to the original one between the two vertical sides and the fluid motion is determined by the balance between buoyant, viscous, and magnetic forces. A solution in the form of Fourier series is possible. However, in the limit as $\text{Ha} \rightarrow \infty$ such a solution is of little help, as it would require a large number of terms for convergence to be attained. Consequently, following Bühler's⁵ three-dimensional analysis in a rectangular duct and the analysis presented by Garandet *et al.*²² for a slightly different flow arrangement, we obtain an asymptotic solution that is valid in the limit of high Ha . It consists of a core section that occupies the central cavity region away from the four walls, where viscous effects are negligible, and two pairs of thin boundary layers each one adjacent to one of the two pairs of cavity walls, Fig. 2. It should also be pointed out that, due to the negligible effect of inertia, this flow arrangement is stable with respect to two-dimensional perturbations. A similar approach has been employed by Ting *et al.*⁷ for the identification of the solution structure in the case of fully developed pressure driven flow through a rect-

angular duct at high Ha . In that case the basic flow structure also consists of a core flow and the two pairs of side and Hartmann layers near the duct walls, with the difference, however, that the basic vorticity field lies in the cross-sectional plane of the duct and is restricted within the side layers. That particular flow structure is subject to three-dimensional instabilities⁷ leading to a quasi-two-dimensional vortical structure,⁸ with the vortices remaining aligned with the magnetic field within the side layers of the duct as a result of Joule dissipation.

In this fashion the temperature distribution in the cavity is obtained by solving the diffusion production problem subject to the boundary conditions prescribed in Eq. (11):

$$\nabla^2 T = -S \text{Pr}, \quad T(x, y) = -(\text{Pr } S) \frac{x^2}{2} + \frac{4 + \text{Pr } S_i}{2} x - 1. \quad (40)$$

The pressure and velocity distributions in the core region are obtained by dropping viscous dissipation,

$$\hat{u}_c = 0, \quad \hat{v}_c = -(\text{Pr } S_i) \frac{x^2}{2} + \frac{4 + \text{Pr } S_i}{2} x - (c + 1), \quad \frac{\partial \hat{p}}{\partial y} = c \quad (41)$$

leaving pressure drop c to be determined in the end of the analysis based on a mass balance in the y direction, after the velocity field near the cavity walls has been calculated.

The two layers located in the vicinity of the two vertical walls, perpendicular to the magnetic field, are called Hartmann layers and are characterized by the balance between viscous and magnetic forces. Since transverse velocity \hat{v} and temperature T remain $O(1)$ everywhere in the cavity, from continuity we deduce that the horizontal velocity $\hat{u} = O(\delta)$ inside the Hartmann layers, where δ is a measure of their thickness. Finally, balancing terms in y momentum we obtain the scale of the Hartmann layer $\delta = Ha^{-1}$ and the transverse velocity profile near the left and right walls,

$$\hat{v}_L = (c + 1)(e^{-X_L} - 1), \quad X_L = \frac{x}{Ha^{-1}}, \quad (42)$$

$$\hat{v}_R = (1 - c)(1 - e^{-X_R}), \quad X_R = \frac{1 - x}{Ha^{-1}}.$$

The two layers adjacent to each one of the two horizontal walls are called side layers and are characterized by the balance between pressure drop and viscosity in x momentum. Based on continuity we obtain $\hat{u} = O(\delta^{-1})$, where δ is the thickness of the side layers. Then, x and y momentum give near $y=0$, after proper rescaling,

$$\frac{\partial p}{\partial x} = \frac{\partial^2 U}{\partial Y^2}, \quad \frac{\partial p}{\partial Y} = T - \hat{v}, \quad Y = \frac{y}{Ha^{-1/2}}, \quad (43)$$

$$U = \frac{\hat{u}}{Ha^{1/2}}, \quad p = \frac{\hat{p}}{Ha^{-1/2}}.$$

Introducing the stream function Ψ we end up with the linear problem:

$$\frac{\partial \Psi}{\partial Y} = U, \quad \hat{v} = -\frac{\partial \Psi}{\partial x}, \quad \frac{\partial^4 \Psi}{\partial Y^4} = \frac{dT}{dx} + \frac{\partial^2 \Psi}{\partial x^2} \quad (44)$$

subject to the usual boundary conditions at the cavity walls and a matching condition with the core velocity

$$\begin{aligned} \frac{\partial \Psi}{\partial x}(x=0, Y) &= \frac{\partial \Psi}{\partial x}(x=1, Y) = \Psi(x, Y=0) \\ &= \frac{\partial \Psi}{\partial Y}(x, Y=0) = \frac{\partial \Psi}{\partial Y}(x, Y \rightarrow \infty) = 0. \end{aligned} \quad (45)$$

In this fashion the solution for the horizontal velocity U is obtained in the form of an infinite series

$$U(x, Y) = \sum_{n=1}^{\infty} T_n \left(\frac{2}{n\pi} \right)^{3/2} \cos(n\pi x) e^{-\sqrt{n\pi/2}Y} \sin\left(\sqrt{\frac{n\pi}{2}} Y \right), \quad (46)$$

where T_n are the coefficients of the expansion of the derivative dT/dx in terms of $\cos(n\pi x)$, $n=1, 2, 3, \dots, \infty$.

Finally, upon application of the mass balance across any horizontal line joining the two vertical walls of the cavity the transverse pressure drop, $\partial \hat{p} / \partial y$, can be obtained to leading order:

$$\begin{aligned} 0 &= \int_0^1 \hat{v} dx = \int_0^{\infty} \hat{v}_L dX_L + \int_0^1 \hat{v}_c dx + \int_0^{\infty} \hat{v}_R dX_R \rightarrow \frac{\partial \hat{p}}{\partial y} \\ &= c = 2 + \frac{\text{Pr } S}{12}. \end{aligned} \quad (47)$$

Recovering numerically the above structure is not an easy task, as it involves resolution of the thin layers that are attached to each one of the cavity walls. To this end the numerical methodology presented in the previous section was used for the computation of steady state solutions to the equation set defined by (36)–(39). A 60×60 element mesh was employed with biquadratic Lagrangian basis functions for the temperature and velocity fields, and bilinear basis functions for the pressure. In order to accommodate abrupt changes near the walls the option for a graded mesh was used in the x direction, where the Hartmann layers that scale like Ha^{-1} develop near the two walls, with $X_{\text{fact}}=1.2$. The cases with $Ha=100$ and 400 were examined for liquid lithium, $\text{Pr}=0.0321$, negligible inertia, $\text{Gr}=0$, and with intense internal heating, $S=10^5$. For this range of Ha the dimensionless thickness of the side layers is on the order of 0.05 , whereas that of the Hartmann layers 0.0025 . Consequently, a uniform 60 quadratic element mesh in the y direction is expected to capture the details of the side layers. The Hartmann layers are thinner and therefore more demanding, hence the grading parameter $X_{\text{fact}}=1.2$. In this fashion, the numerical solution captures quite satisfactorily the above asymptotic solution. This is illustrated in Figs. 3(a) and 3(b) where contours of the horizontal velocity $\hat{u}(x, y)$ are shown for $Ha=100$ and 400 , respectively. The thinning of the side layers is accurately captured, their thickness is halved as Ha is quadrupled, while at the same time the magnitude of

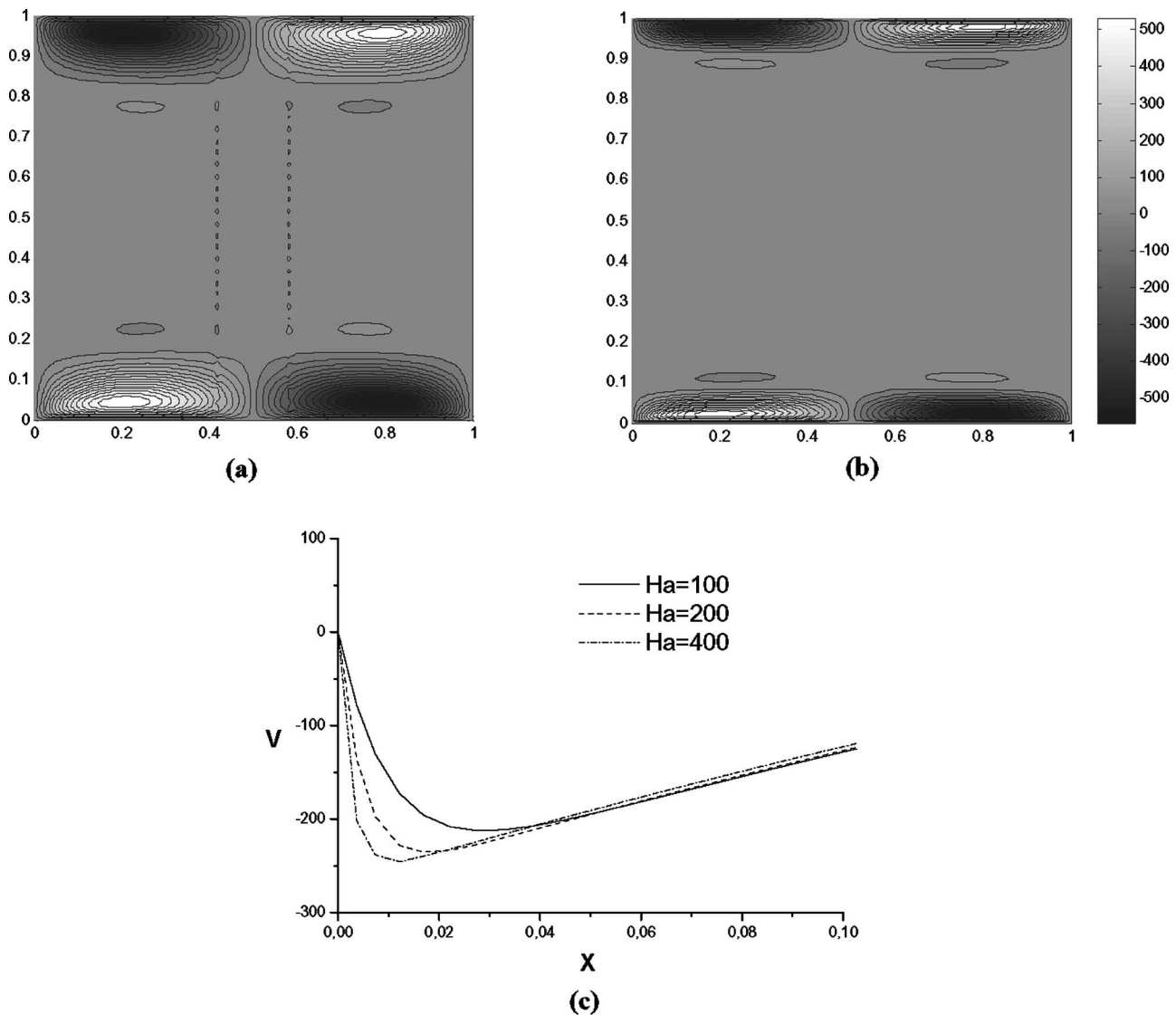


FIG. 3. Numerically calculated contours of the horizontal velocity $\hat{u}(x,y)$ when (a) $Ha=100$ and (b) $Ha=400$ ($Gr=0$, $Pr=0.0321$, $Gr_l=10^5$); (c) Numerically obtained profiles of transverse velocity $\hat{v}(x,y)$ near the left vertical wall when $Ha=100$, 200, and 400.

$\hat{u}(x,y)$ becomes twice as large in them, again as predicted by the asymptotic analysis ($\hat{u} \sim Ha^{1/2}$). The variation of the transverse velocity, \hat{v} , is not shown as clearly when depicted over the entire range of y values, due to the very small size of the Hartmann layers near the vertical walls. For this reason the portion of the profile near the left wall is shown in Fig. 3(c), the one near the right wall being the same and the core region following closely Eq. (41). As can be seen by following the location of the minimum in \hat{v} , albeit not with the same accuracy as for the side layers, there is a clear tendency for the thickness of the Hartmann layer to be inversely proportional to Ha , while \hat{v} remains the same in magnitude. This inverse proportionality of \hat{v} has also been captured in the three-dimensional simulations presented elsewhere.¹⁵ Similar observations can be done with respect to all aspects of the solution. In particular when $Ha=400$ the transverse pressure drop, $\partial \hat{P} / \partial y$, is calculated numerically to be very close to 270, i.e., the value predicted by Eq. (47) for the parameter values of the simulation. It should also be

noted that the above numerical results vary very little when Gr increases to become as large as 100, due to the very small ratio $Gr^{1/2}/Ha^2$.

VI. RESULTS AND DISCUSSION FOR FINITE Ha

Considering a square cavity with length size on the order of 1 cm and a temperature difference on the order of 1 K across the two vertical plates, Gr is estimated to be 5×10^4 for liquid lithium at roughly 300 °C, whereas Ha ranges from 5 to 500 when the magnetic field intensity B_0 varies between 0.1 and 1 T. The above parameter values determine the range of the parametric investigation that was conducted in the present study. In addition, in order to accommodate flow situations where large amounts of heat are being released, as is the case with the tritium breeding reaction, S values as large as 2×10^5 were used in the simulations. Due to the large amount of heat that is released in some of the simulations, properties of the operating fluid may deviate

from their values obtained for 300 °C. Nevertheless, as a first attempt to study the system dynamics under the influence of a large heat load we neglect temperature variations of the thermophysical properties involved in the problem formulation. This does not constitute a significant restriction on the validity of our formulation, since the Pr number of lead-lithium coolants (e.g., Pb-17%Li) acquires relatively low values²³ in the temperature range 300–600 °C, ranging between 0.05 and 0.02. In the following, steady state solutions are obtained for the above parameter range and their stability is investigated in Sec. VI A, in the manner described in the penultimate section. The neutral stability curves separating steady state from periodic solutions are obtained in the (Gr, S) plane as a function of Ha. The results of steady and dynamic simulations, in the form of bifurcation diagrams, are presented in Sec. VI B. Unless otherwise specified 30×30 and 60×60 biquadratic Lagrangian meshes were used in the simulations discussed below.

A. Stability analysis

The case with vanishing heat production, corresponding to $S=0$, was first examined in terms of its stability as Gr increases, in the absence of a magnetic field. The temperature field acquires its maximum value at the right vertical wall and the stream function exhibits a single recirculation cell. This pattern of steady unicellular recirculatory flow persists as Gr increases with the temperature isolines becoming curved upwards indicating a tendency for hot material to occupy the upper portion of the cavity, Fig. 4(b), as the effect of buoyancy is intensified. At the same time the recirculation vortex also becomes skewed upwards, Fig. 4(a). The steady state solution remains stable for the entire range of Gr, as indicated by the real part of the eigenvalues which remains negative.

As the amount of heat being volumetrically released increases the temperature field acquires a maximum in the center region of the cavity and a bicellular recirculation pattern is established, Figs. 5(a) and 5(b). Fluid is essentially pumped out of the colder left and right vertical sides moving towards the bottom while hotter fluid from the center of the cavity is rising to the top, thus forming two counter-rotating vortices. As Gr increases this flow structure persists, with the mixing effect of the two vortices being intensified and the asymmetry between the left and right region of the cavity being accentuated as the entire stream line structure is tilted towards the colder left side. This is a result of the increasing effect of buoyancy on the flow structure that is also reflected in the lower temperatures observed in the cavity as Gr increases, see also Figs. 5(b), 5(d), and 5(f). In addition, as illustrated by the stream line structure, Figs. 5(a), 5(c), and 5(e) as Gr increases a larger part of the fluid in the cavity participates in the circulatory motion. In fact, additional smaller recirculation cells appear near the bottom of the cavity further decreasing the average temperature of the cavity, Figs. 5(d) and 5(f). Interestingly enough, further increase of Gr reinstates the symmetry of the system, as illustrated in Fig. 6 for $Gr \geq 50\,000$. The dynamic behavior of the system in this parameter range is discussed in the next section.

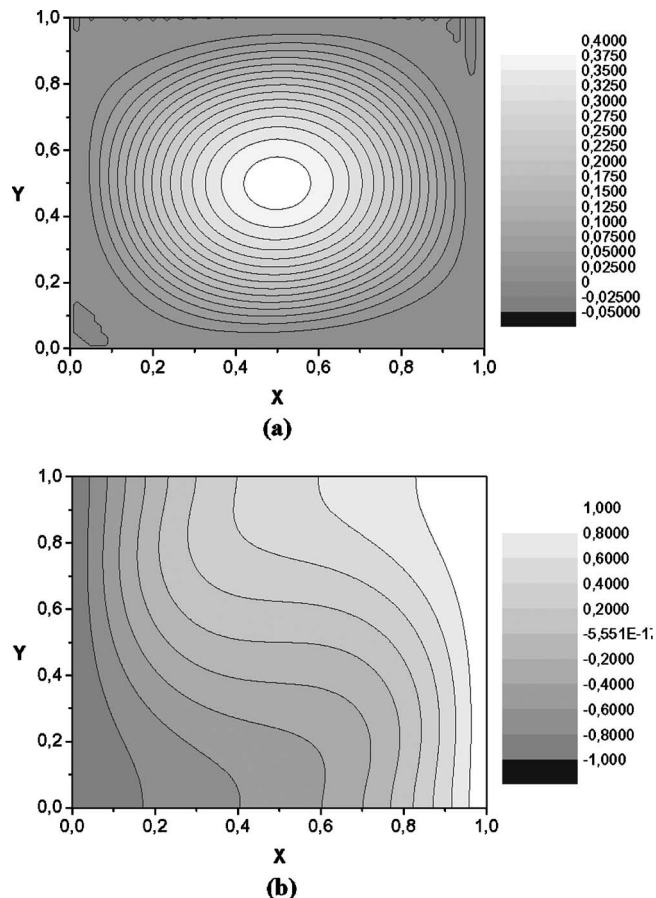


FIG. 4. (a) Streamline and (b) temperature contours, for the case with $Gr=10^5$, $S=0$, and $Ha=0$.

A concomitant effect of the growing asymmetry is the loss of stability of the steady state solution when $Gr \approx 5800$. This is illustrated in Table I showing the real and imaginary parts of the six largest eigenvalues based on their real parts, as Gr increases. Numerical convergence is also examined by repeating the calculation with a 60×60 mesh. As can be observed by inspection of Table I, accuracy of two or three significant digits has been attained with the Arnoldi method that was employed, especially for the imaginary part that bears significance on the time scales exhibited by the dynamic simulations. The first eigenvalue that crosses the real axis to acquire a positive real part does so for $Gr \approx 5\,800$ and has a nonzero imaginary part, $\omega_{1i} \approx 64$, which is indicative of a Hopf bifurcation leading to a periodic solution.^{18,19} This is better illustrated in a bifurcation diagram in the parameter space, e.g., one depicting the average cavity temperature versus Gr, as shown in the next subsection where the steady and dynamic simulations are cross-examined. As Gr is further increased another eigenvalue of the steady state solution acquires a positive real part, $Gr \approx 10\,000$, in the same fashion as the first one, i.e., maintaining a nonzero imaginary part. Subsequently a third eigenvalue crosses the real axis, $Gr \approx 13\,500$. In both cases complex eigenvalues are obtained in pairs of complex conjugates. The effect of the second, the third as well as the rest of the unstable eigenvalues on the dynamics of the system is not as important since the steady

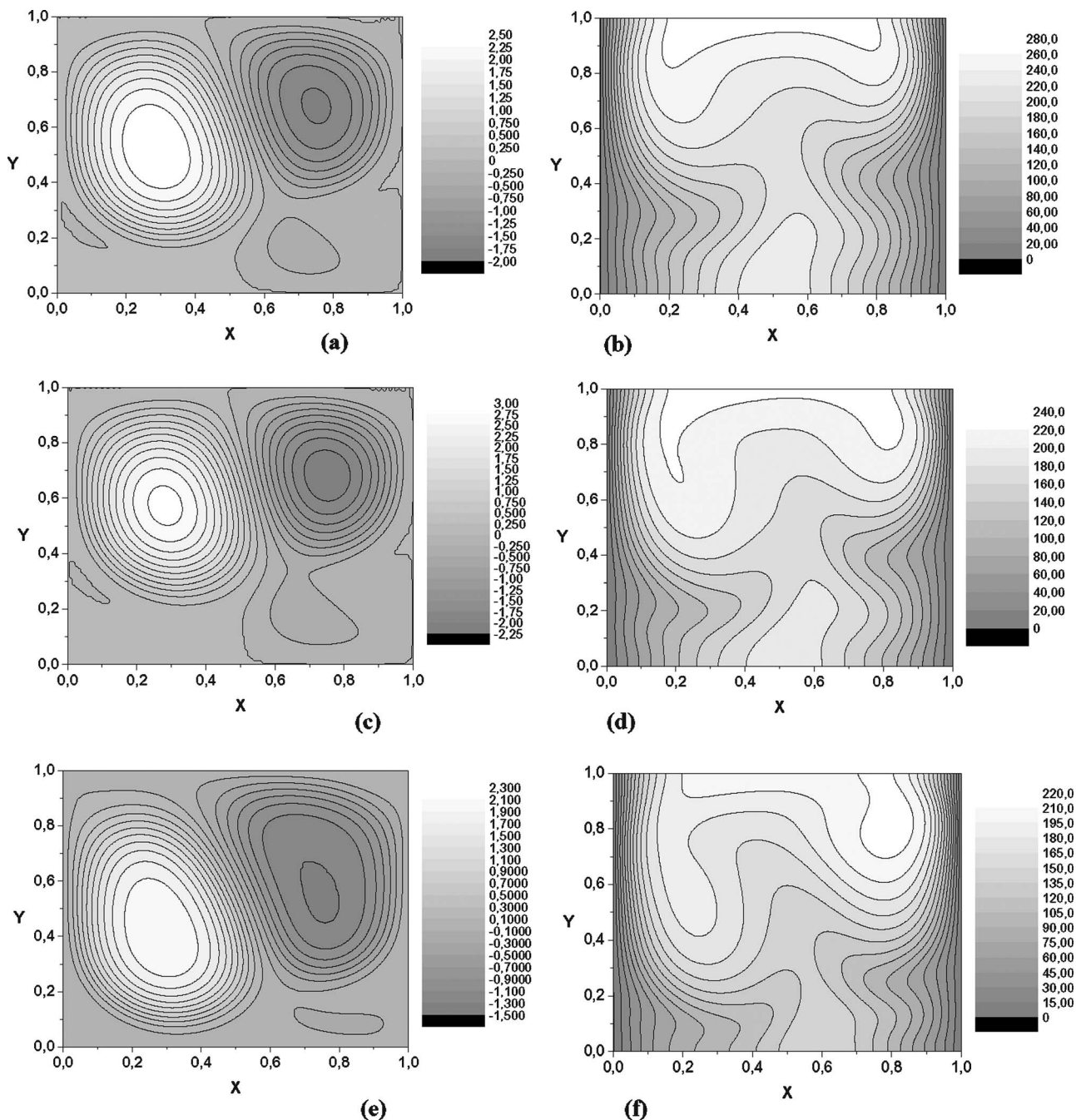


FIG. 5. Streamline and temperature contours for (a) and (b) $Gr=6\,000$, (c) and (d) $Gr=15\,000$, and (e) and (f) $Gr=30\,000$; $S=10^5$ and $Ha=0$.

state solution is already unstable. Nevertheless, they affect the transient behavior of the system by introducing additional time scales before the system eventually settles to its periodic steady state. This is also better explained in the next subsection. The existence of Hopf bifurcations in differentially heated cavities has been observed by other investigators as well.²¹

Further increase of the amount of heat that is being released, i.e., increasing S , destabilizes the system in the sense that it decreases the critical value of Gr_{cr} for which the steady state solution first becomes unstable. More specifically, heat production generates very large temperature gradients in the cavity, Fig. 7(b), and consequently further in-

creases the effect of buoyancy in the flow arrangement for given Gr , Fig. 7(a). Thus, it affects the system behavior and stability in the same fashion as increasing Gr , i.e., introduces asymmetry and destabilizes the steady state. In fact, when $S=2 \times 10^5$ the critical value of Gr becomes, $Gr_{cr} \approx 2400$. Imposition of the magnetic field has the opposite effect from heat production since it stabilizes the system by mitigating the effect of buoyancy. Hot and cold fluid masses remain segregated at the top and bottom regions of the cavity, respectively, leading to a more symmetric flow configuration, Figs. 7(c) and 7(e) and, consequently, to higher temperatures, Figs. 7(d) and 7(f), in the cavity. Table II gives the evolution of the six most important eigenvalues with Ha , in terms of

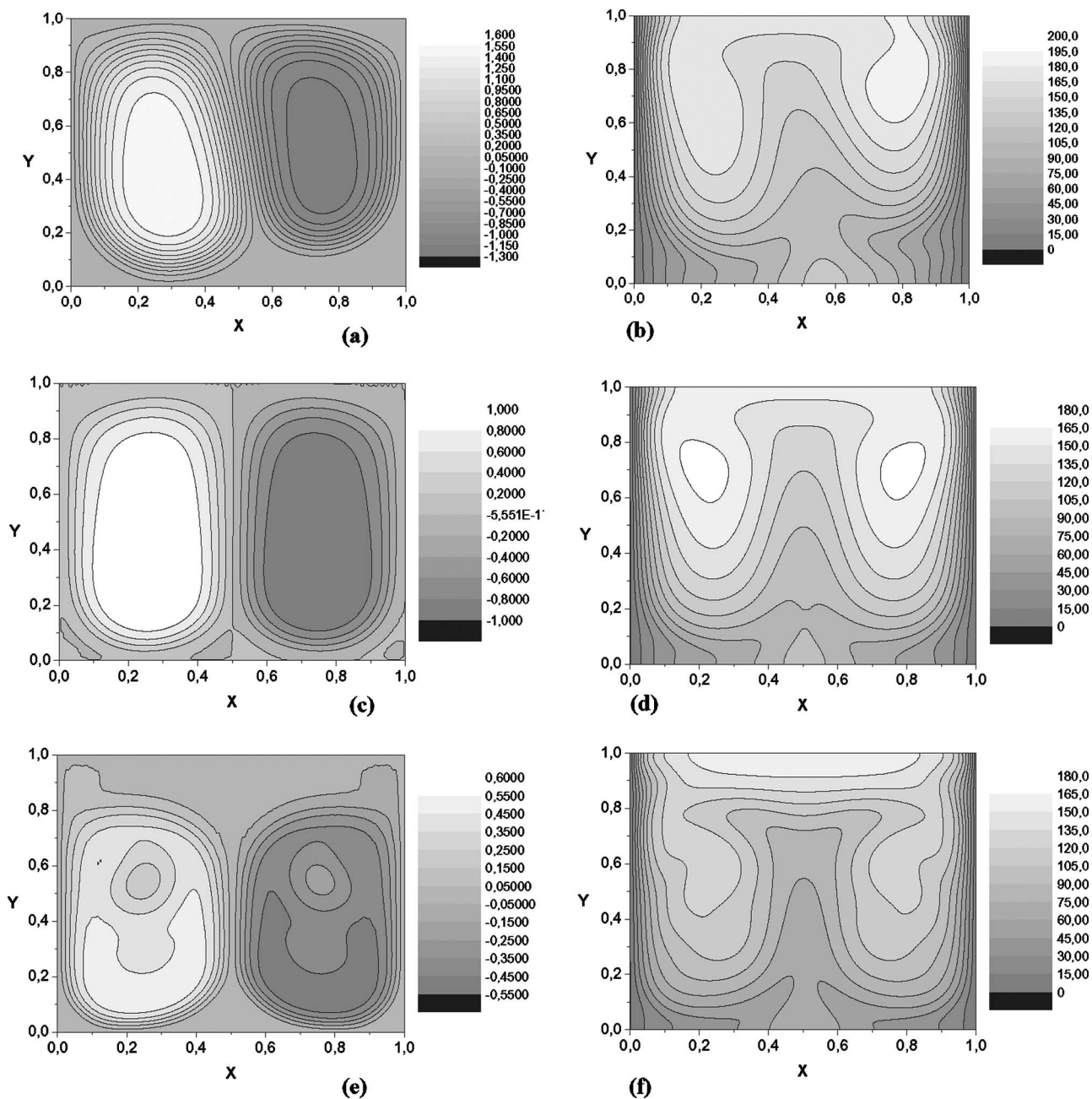


FIG. 6. Streamline and temperature contours for (a) and (b) $Gr=50\,000$, (c) and (d) $Gr=10^5$, and (e) and (f) $Gr=10^6$; $S=10^5$ and $Ha=0$.

the magnitude of their real part. Numerically calculated eigenvalues, obtained with a 30×30 and a 60×60 mesh are shown. As expected increasing Ha gradually stabilizes all the unstable eigenvalues, forcing their real part to drop below zero, until the flow is completely stabilized when $Ha=20$. In fact this is already the case when $Ha \approx 12$. It should be noted, that the eigenvalue that is last stabilized is the one that first became unstable.

The eigenvectors corresponding to the first two eigenvalues that become unstable have been checked for convergence with a 30×30 and a 60×60 mesh. The stream line pattern in the cavity, as obtained via the calculated eigenvector when $Gr=5\,800$, $S=10^5$, and $Ha=0$, is more or less centered with respect to a vertical line going through the center of the cavity. This is reflected in the dynamic behavior of the peri-

odic solution that emerges from this Hopf bifurcation point, which will be seen to periodically go through a more symmetrical configuration of the streamline pattern that is centered in the middle of the cavity. The second eigenvector that crosses the real axis is calculated at the critical value of $Gr \approx 10\,000$ when $S=10^5$ and $Ha=0$, with a 60×60 mesh. This one corresponds to a displaced pattern for the recirculation cells. This stability pattern is in agreement with previous studies on free convection in cavities.²¹ In fact, in the latter study it was shown that, for a cavity with aspect ratio $A=2$ and at relatively low values of Pr ($Pr < 0.71$), the steady state configuration first loses stability owing to the appearance of a symmetric mode followed by an antisymmetric mode. In the context of the present study, the most unstable eigenvectors that arise as Ha increases, for the range of Ha

TABLE I. Evolution of the six largest eigenvalues, based on their real part, with Gr and their convergence for a 30×30 and a 60×60 biquadratic finite element mesh; $S=10^5$, $Ha=0$, $Pr=0.0321$.

S=10 ⁵ , Ha=0, Pr=0.0321, 30×30 biquadratic finite element mesh									
Gr=4 000		Gr=6 000		Gr=8 000		Gr=10 000		Gr=12 000	
Real	Imaginary	Real	Imaginary	Real	Imaginary	Real	Imaginary	Real	Imaginary
-2.919	±17.331	0.704	±64.205	3.629	±62.121	5.301	±60.284	6.212	±58.451
-3.573	±38.842	-1.677	±17.644	-0.643	±17.584	0.0547	±17.321	0.491	±16.962
-3.629	0.0	-2.835	±37.425	-2.508	0.0	-2.203	0.0	-1.967	0.0
-4.259	±4.250	-2.937	0.0	-2.806	±35.796	-2.922	±34.215	-2.864	0.0
-4.464	±66.676	-3.944	0.0	-3.473	0.0	-3.127	0.0	-3.104	±32.681
-4.649	0.0	-4.104	±4.968	-3.837	±5.328	-3.458	±5.319	-3.115	±5.120
S=10 ⁵ , Ha=0, Pr=0.0321, 60×60 biquadratic finite element mesh									
Gr=4 000		Gr=6 000		Gr=8 000		Gr=10 000		Gr=12 000	
Real	Imaginary	Real	Imaginary	Real	Imaginary	Real	Imaginary	Real	Imaginary
-2.897	±17.264	0.423	±64.044	3.313	±61.935	4.967	±60.041	5.923	±58.200
-3.591	0.0	-1.721	±17.545	-0.716	±17.476	-0.020	±17.222	0.419	±16.889
-3.731	±38.792	-3.024	±37.347	-2.499	0.0	-2.203	0.0	-1.976	0.0
-4.190	±4.240	-2.920	0.0	-2.991	±35.734	-3.110	±34.141	-2.839	0.0
-4.623	±66.564	-3.922	0.0	-3.449	0.0	-3.103	0.0	-3.054	±5.118
-4.637	0.0	-4.006	±4.935	-3.754	±5.277	-3.387	±5.315	-3.245	±32.654

that was investigated $0 \leq Ha \leq 20$, evolve in the manner described above. In fact, when $Ha \geq 12.5$ the most unstable eigenvectors become more symmetric with additional smaller recirculation cells. An interesting phenomenon that is observed as Ha increases from 15 to 20 has to do with the fact that there is a change in the order by which the two most unstable eigenvalues cross the real axis. The one that crosses second in the range $12.5 \leq Ha \leq 15$ grows faster when $Ha = 20$ and it becomes the most unstable one. This is associated with a minimum in the frequency of the oscillatory solution, as predicted by the imaginary part of this particular eigenvalue at neutral stability, which now turns to acquiring higher values. Owing to the large Ha and Gr numbers an 80×80 biquadratic finite element mesh was required in order to ascertain a three significant accuracy for the imaginary part at the bifurcation point and a better description of the two competing eigenvectors. Table III provides the corresponding values for Gr_{cr} and ω_0 as a function of Ha when $S=10^5$.

For completeness a neutral stability diagram has been constructed in the (Gr, S) plane for three different values of Ha , namely, 0, 10, and 20, showing the curve $S=S(Gr_{cr})$ separating regions where the steady state solution is stable from those where it loses stability, $Gr > Gr_{cr}$, to a periodic solution, Fig. 8. Regions in the plane lying above each critical curve indicate loss of stability. Below the critical curve steady state solutions are possible. A very wide range of parameters has been covered. Very large values of Ha are not included in this graph, since in the context of two-dimensional disturbances for fixed Gr the steady flow is stable for high enough Ha . The graph clearly illustrates this fact, in the form of elevated critical curves with respect to the case where the magnetic field is absent, as well as the destabilizing effect of increased buoyancy or heat generation. The

actual data points have been obtained by the method of intersection, i.e., the eigenvalues of the steady state solution are monitored by setting the S , Pr , and Ha while varying Gr until the real part of one of the eigenvalues crossed the real axis. The minimum interval that was used in Gr varied from 100, for relatively low values of Gr_{cr} , up to 1000 when Gr_{cr} became very large. The results were checked using a 30×30 and 60×60 element mesh when $Ha < 15$, whereas a 80×80 mesh was employed in order to check the validity of calculations at high Ha . The high Ha or low Gr regime that was examined asymptotically in the previous section corresponds to the far left region in the neutral stability diagram and is always stable for two-dimensional disturbances. The stabilizing effect of Ha and the increase in Gr_{cr} with increasing Ha was also identified for the horizontal Bridgeman configuration with the magnetic field aligned with gravity.²⁴ Here the Lorenz force directly opposes buoyancy thus we expect a more pronounced effect by the magnetic field.

B. Bifurcation diagrams

As a first attempt to correlate asymmetry and instability, the graph of $Nu_L - Nu_R$ vs Gr is plotted in Figs. 9(a)–9(c) when $S=10^5$ and $Ha=0, 10$, and 20, respectively. Increasing Gr introduces asymmetry to the steady state solution and this is reflected in the difference in the heat that is removed through the two sides of the cavity. Most of it is removed through the colder left side of the cavity, hence $\Delta Nu = Nu_L - Nu_R$ is positive. As is also shown in Fig. 9 the difference ΔNu is initially an increasing function of Gr , indicating the enhancement of asymmetry as the recirculation is intensified in the cavity. However, as Gr increases the level of asymmetry acquires a maximum for some value of Gr , e.g.,

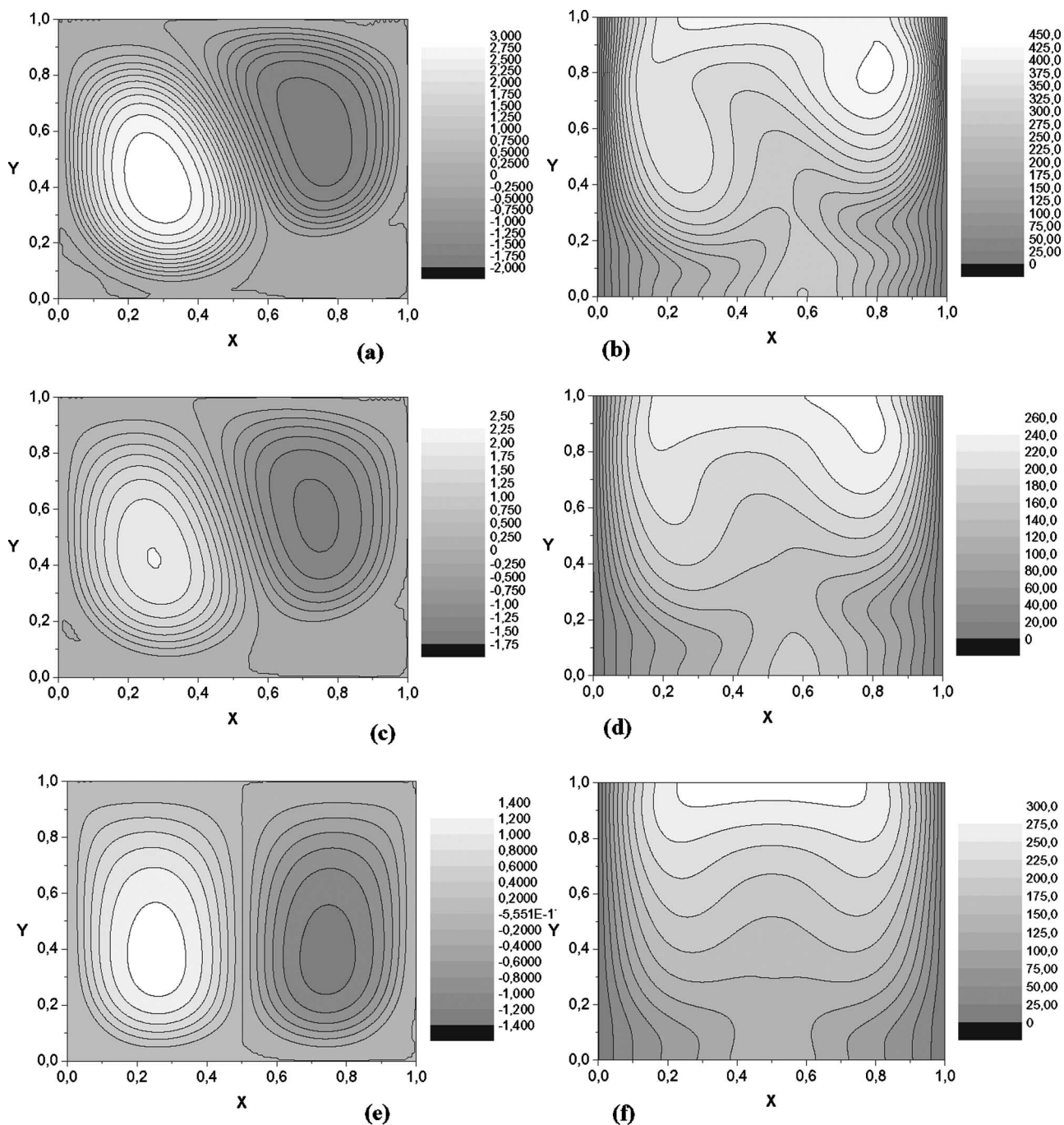


FIG. 7. Streamline and temperature contours for (a) and (b) $S=2 \times 10^5$ and $Ha=0$, (c) and (d) $Ha=10$ and $S=10^5$, and (e) and (f) $Ha=20$ and $S=10^5$; $Gr = 15\,000$.

$Gr \approx 18\,000$ when $Ha=0$ and $S=10^5$, and subsequently it starts decreasing. It should be stressed that it is within this region of the bifurcation diagram that the steady state solution first becomes unstable, e.g., $Gr \approx 5\,800$ when $Ha=0$ and $S=10^5$. After this region the asymmetry forms a second weaker maximum until it reaches an asymptotic state, $Gr \rightarrow \infty$, characterized by the kind of contours shown in Fig. 6. This is a region that exhibits a different type of symmetry when compared to the flow arrangement in the presence of a magnetic field or to the case of negligible Gr . In the latter case the cavity is characterized by a quadratic temperature profile, as a result of the balance between the diffusion and

production terms, and two recirculation vortices symmetrically located at the left and right semiplanes of the cavity. In the large Gr regime the temperature field is gradually becoming uniform in the core region, see Figs. 6(d) and 6(f), with two narrow boundary layers forming adjacent to the two vertical sides of the cavity, through which heat is being removed. As Gr increases the two recirculation cells are progressively confined near the bottom of the cavity while the temperature field becomes stratified at the top. Throughout this process the average temperature of the cavity keeps decreasing as a result of the effect of recirculation. This pattern persists in the range of moderate Ha with the large Gr branch

TABLE II. Evolution of the six largest eigenvalues, based on their real part, with Ha and their convergence for a 30×30 and a 60×60 biquadratic finite element mesh; S=10⁵, Gr=15 000, Pr=0.0321.

S=10 ⁵ , Gr=15 000, Pr=0.0321, 30×30 biquadratic finite element mesh					
Ha=0		Ha=10		Ha=20	
Real	Imaginary	Real	Imaginary	Real	Imaginary
7.068	±55.764	0.899	±43.638	-4.185	±9.419
2.016	±85.494	-1.946	±4.314	-5.704	0.0
0.898	±16.396	-1.979	0.0	-6.513	±1.265
-1.699	0.0	-2.624	±72.283	-6.623	±29.411
-2.587	0.0	-2.829	±34.545	-6.785	0.0
-2.754	±4.564	-4.493	±57.709	-7.785	±24.128

S=10 ⁵ , Gr=15 000, Pr=0.0321, 60×60 biquadratic finite element mesh					
Ha=0		Ha=10		Ha=20	
Real	Imaginary	Real	Imaginary	Real	Imaginary
6.716	±55.464	0.696	±43.246	-4.172	±9.450
1.790	±85.204	-1.960	±4.346	-5.730	0.0
0.724	±16.326	-1.971	0.0	-6.501	±1.257
-1.711	0.0	-2.786	±71.846	-6.620	±29.290
-2.556	0.0	-2.865	±34.556	-6.770	0.0
-2.646	±4.582	-4.632	±57.810	-7.773	±24.107

characterized by similar type of contours as those in Figs. 6(c)–6(f). A more detailed description of the steady state solution branch as Gr→∞ was not pursued in the present study since, as shown by the stability analysis and confirmed by dynamic simulations, it is a branch that loses its stability to a periodic solution for a much smaller value of Gr.

An interesting peculiarity of the bifurcation diagram is the appearance of a hysteresis loop when Ha=0, in the form of two consecutive limit points within a narrow interval of Gr, Gr≈51 600 and Gr≈50 500, before the branch eventually turns to acquire its large Gr behavior. It arises when the real eigenvalue with the smallest real part crosses zero to become positive. Steady state solutions belonging to this branch are obtained with the help of the eigenvector corresponding to the unstable eigenvalue. Employment of arc-length continuation would provide a better description of this region but it was not pursued here since the corresponding steady state solutions are unstable. The hysteresis loop is eliminated as Ha increases, see Fig. 9(b) for Ha=10, but the large Gr part of the branch is present with similar characteristics. This pattern persisted for higher heat production rates,

i.e., for larger S values such as S≤2×10⁵, but it was modified for the range of smaller S and larger Ha values, e.g., S≤10⁴ or 12.5≤Ha≤20, that was investigated. In particular, when the intensity of the magnetic field is increased or the heat production level reduced the second maximum in ΔNu tends to be eliminated and the bifurcation diagram exhibits the first maximum at much higher Gr values, as in Fig. 9(c) that is characteristic of high Ha behavior or Fig. 9(d) that is characteristic of low but finite heat production levels, before the large Gr behavior is recovered.

Clearly then, there is a correlation between stability and symmetry, that has been pointed out elsewhere²⁵ as well in the context of forced and free magnetohydrodynamic convection. Monitoring the evolution of the first two eigenvalues

TABLE III. Evolution of the critical Gr, Gr_{cr}, and the corresponding frequency, ω₀, at the Hopf bifurcation with increasing Ha; S=10⁵.

S=10 ⁵		
Ha	Gr _{cr}	ω ₀
0	5 800	64.3
5	6 000	60.5
10	10 000	47.0
15	70 000	24.3
20	128 000	35.9

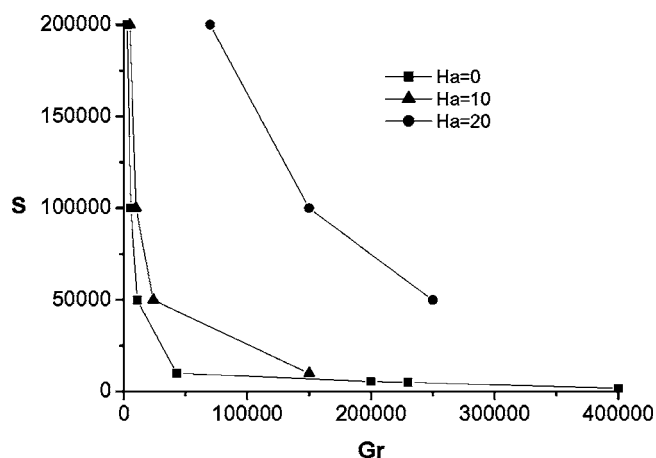


FIG. 8. Neutral stability diagram for two-dimensional free convection of liquid lithium, Pr=0.0321, in a square cavity in the presence of a magnetic field; Ha=0, 10, and 20.

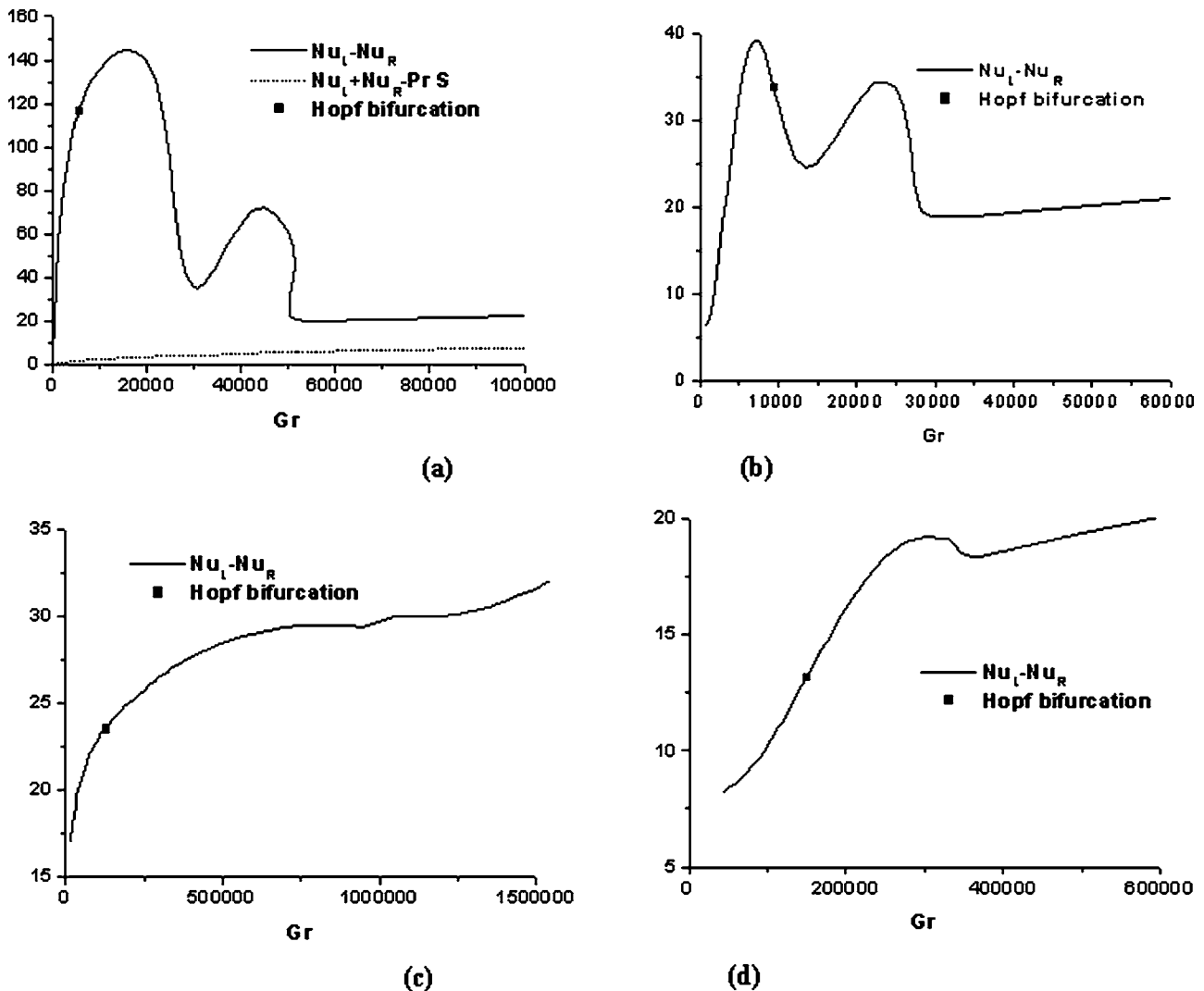


FIG. 9. Evolution of the difference in the amount of heat removed through the left and right-hand sides of the cavity when (a) $Ha=0$, (b) $Ha=10$, (c) $Ha=20$ ($S=10^5$), and (d) $Ha=10$ with $S=10^4$.

that become unstable we can identify the correlation between loss of stability and symmetry. Eigenvalue calculations in the range of Gr determined by the first bifurcation and a little before the large Gr regime, i.e., $5\,500 < Gr < 40\,000$ when $Ha=0$ and $S=10^5$ or $9\,500 < Gr < 30\,000$ when $Ha=10$ and $S=10^5$, indicate that the real part of the most unstable mode starts decreasing after forming a maximum in which case it is overtaken by the second most unstable eigenvalue. Tables IV(a) and (b) show the evolution of the most unstable eigenvalues in the appropriate parameter range when $Ha=0$ and 10, respectively. A similar behavior is obtained for the case with $Ha=20$ with the understanding that the most unstable eigenmode is now different. As it turns out, further increase of Gr may either completely stabilize the mode that first became unstable, $Ha=0$, or reactivate the instability, $Ha=10$ and 20, after its real part goes through a minimum. In all cases examined, however, an increase in Gr was always associated with the appearance of more unstable eigenvalues, at least for the parameter range that was investigated.

C. Dynamic simulations

The bifurcation diagrams presented so far contain the steady state branch that was shown to become unstable due to the onset of periodic oscillations. In order to examine the nature of the emerging Hopf branch one has either to resort to weakly nonlinear analysis or perform dynamic simulations. Owing to the wider range of validity of the later we decided to conduct dynamic simulations in the parameter range covered by the stability analysis and the bifurcation diagrams. Most of the simulations were performed near the bifurcation point in order to establish the criticality of the new branch, i.e., determine whether the new branch is super or subcritical. In order to compare the efficiency of heat removal in the different solution branches the average cavity temperature is also used as the bifurcation parameter.

Despite the fact that as Gr increases the level of symmetry of the steady state solution may vary, the average temperature of the cavity is constantly decreasing, Fig. 10, as a result of the recirculation process that involves an ever larger

TABLE IV. (a) Evolution of the six largest eigenvalues, based on their real part, with Gr for a 60×60 biquadratic finite element mesh; S=10⁵, Ha=0, Pr=0.0321. (b) Evolution of the three largest eigenvalues, based on their real part, with Gr for a 60×60 biquadratic finite element mesh; S=10⁵, Ha=10, Pr=0.0321.

(a) S=10 ⁵ , Ha=0, Pr=0.0321, 60×60 biquadratic finite element mesh											
Gr=18 000		Gr=20 000		Gr=25 000		Gr=30 000		Gr=40 000		Gr=60 000	
Real	Imaginary	Real	Imaginary	Real	Imaginary	Real	Imaginary	Real	Imaginary	Real	Imaginary
7.164	±52.820	7.352	±51.150	7.177	±47.860	5.865	±45.728	3.786	±40.053	3.237	±43.47
3.791	±82.240	4.535	±80.323	4.731	±76.011	3.033	±71.455	3.641	±63.950	3.186	±58.0
0.717	±15.729	0.5650	±15.319	-0.366	±1.934	1.172	±53.617	4.038	±49.900	2.663	±29.24
-1.500	0.0	-1.387	0.0	-0.698	±14.005	0.118	±76.761	0.732	±68.821	2.587	±62.16
-2.241	±3.816	-1.872	±3.155	-0.809	±39.167	-0.926	0.0	1.535	±32.904	2.510	±45.05
-2.403	0.0	-2.275	±44.500	-1.053	±62.823	-0.155	±3.571	-1.229	0.0	-0.620	±26.91

(b) S=10 ⁵ , Ha=10, Pr=0.0321, 60×60 biquadratic finite element mesh									
Gr=10 000		Gr=14 000		Gr=20 000		Gr=22 000		Gr=24 000	
Real	Imaginary	Real	Imaginary	Real	Imaginary	Real	Imaginary	Real	Imaginary
-0.086	±47.017	0.676	±43.952	0.261	±39.260	0.176	±37.471	0.251	±35.677
				-1.083	±52.266	-0.122	±51.170	0.482	±50.208

part of the cavity fluid, except for the very small viscous boundary layers near the walls. However, a good part of this solution branch, e.g., $Gr > 1.5 \times 10^5$ for $S=10^5$ and $Ha=20$, is unstable and consequently of little practical use as far as optimizing heat removal is concerned. For this parameter range, dynamic simulations are necessary in order to determine the long time behavior of the system, in terms of the appropriate bifurcation variables, and compare it with the steady state solution. In particular, the time evolution of the average cavity temperature for six different values of Gr, $Gr=5\ 950, 6\ 000, 6\ 500, 10\ 000, 15\ 500,$ and $25\ 000$, is shown in Figs. 11(a)–11(f), respectively; $S=10^5, Ha=0$. Initial conditions are obtained from steady state solutions at different Gr values. For Gr values below 5 800, even for large initial disturbances, the system eventually settles to the steady state solution. This is a result of the stability of the steady state solution in this parameter range. When the dy-

amic simulation is repeated with Gr set to a value that lies beyond the Hopf bifurcation point at $Gr \approx 5\ 800$, the system initially attempts to acquire the steady state solution, Figs. 11(a) and 11(b), forming a plateau in T_{AV} . However, as time elapses the dynamics are gradually dominated by the periodic mode indicated by the stability analysis that was presented above and the system eventually exhibits a steady oscillatory motion. As Gr further increases, Figs. 11(c)–11(e), the plateau is eliminated but the system dynamics is still eventually dominated by the most unstable Hopf mode. Close examination of the evolution of the average temperature and the rest of the quantities describing the system, e.g., temperature and stream function contours, reveals that the period of the oscillations is very close to the prediction of stability analysis with a tendency to gradually increase as the departure from the bifurcation point grows, a result familiar from weakly nonlinear theory. In particular, the period of the steady oscillations is calculated to be in the range $0.098 \leq T_0 \leq 0.12$ when $5950 \leq Gr \leq 15500$, whereas the value predicted by stability analysis is $2\pi/64.3=0.098$, where $\sigma_{1i}=64.3$ the imaginary part of the eigenvalue whose real part crosses first the real axis when $Gr \approx 5800$, see also Table I. In addition, the time needed for the periodic nature of the system dynamics to be manifested decreases with increasing departure from the critical point, Figs. 11(a)–11(c), a result that is also expected by weakly nonlinear theory. Another important aspect of the dynamic simulations is the effect of subsequent unstable eigenvalues. More specifically, they are seen to affect the transient response of the system while the long time behavior is dominated by the most unstable eigenvalue. This is clearly illustrated in simulations with Gr in the order of 10^4 , in which case two unstable eigenvalues exist as shown in Table I, where as soon as the average cavity temperature almost establishes a plateau near the steady state value for $Gr=10\ 000$, it starts exhibiting an oscillatory behavior characterized by a beat between the first

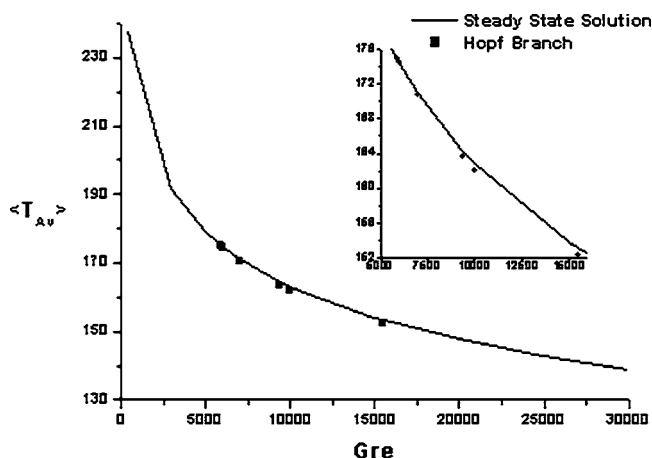


FIG. 10. Bifurcation diagram of the steady state and Hopf branches in terms of the average cavity temperature, $\langle T_{AV} \rangle$, as a function of Gr; $S=10^5, Ha=0$.

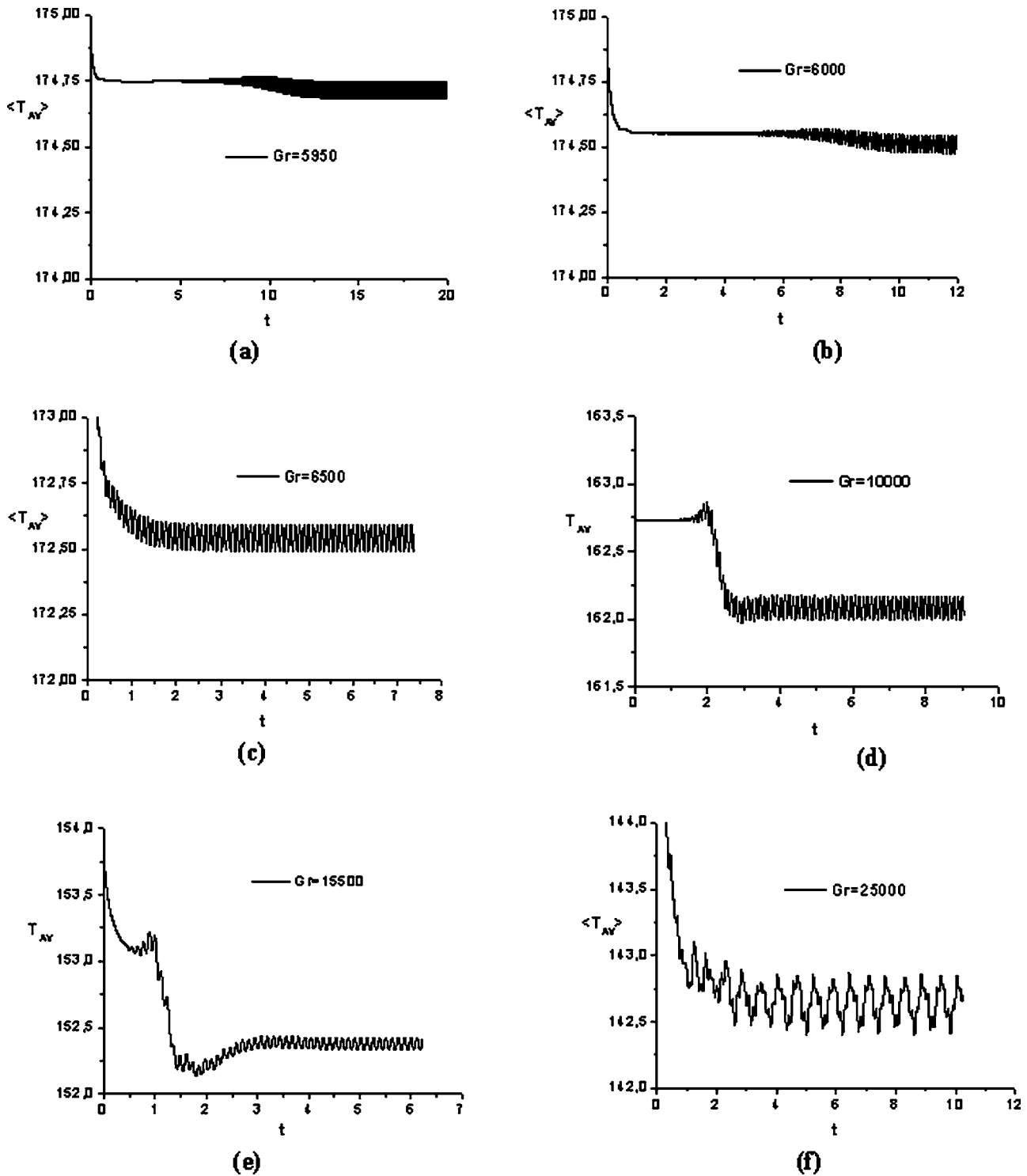


FIG. 11. Dynamic evolution of the average cavity temperature T_{AV} for $Ha=0$, and $S=10^5$ when (a) $Gr=5\,950$, (b) $Gr=6\,000$, and (c) $Gr=6\,500$, with initial condition at the steady state solution for $Gr=5\,900$, (d) $Gr=10\,000$ with initial condition at the steady state solution for $Ha=0.5$, (e) $Gr=15\,500$ with initial condition at the steady state solution for $Gr=15\,000$, and (f) $Gr=25\,000$ with initial condition at the steady state solution for $Gr=20\,000$.

two modes that become unstable. In particular, Fig. 11(d), there are two time scales evident in the system response, the first one belonging to the most unstable mode, $T_0 \approx 0.11$, and the second one determined by the mode that crosses second the real axis, $T_1 \approx 0.35$. As can be gleaned from Table I the imaginary part of this mode is roughly $\sigma_{2i} = 17.2$ when it crosses. Eventually, however, the dynamic state of steady

oscillations is reached with a period that is close to that of the most unstable mode, namely, $T \approx 0.11$. As will also be seen in the following, this effect is intensified as Gr further increases, Figs. 11(e) and 11(f), until, for even larger values of Gr , a steady oscillatory pattern is no longer observed owing to the increasing effect of additional unstable modes. Clearly then, the periodic branch emerges as a supercritical

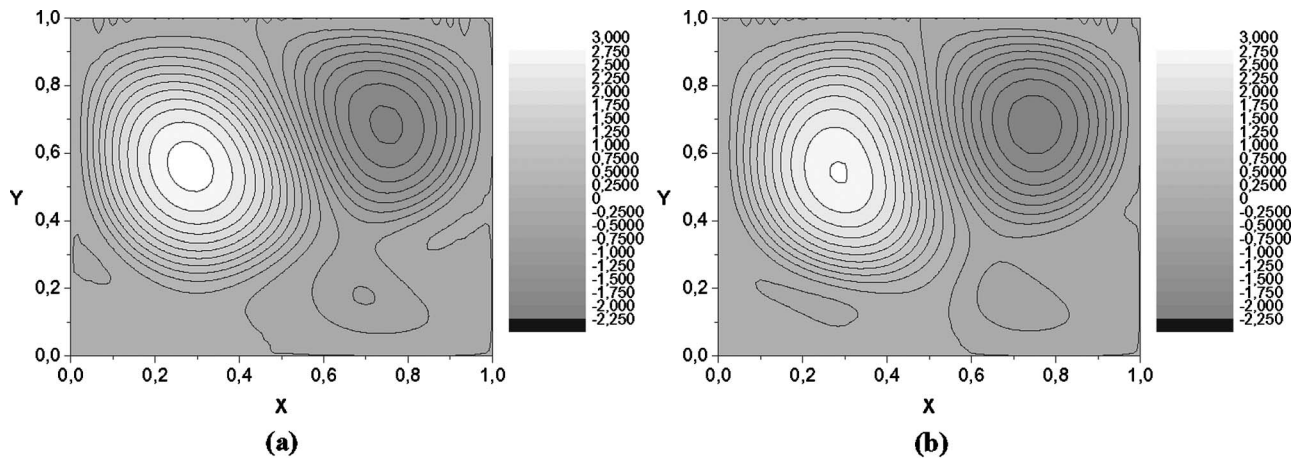


FIG. 12. Stream function snapshots at the beginning and in the middle of the steady periodic motion for the case with $Gr=7\,000$, $S=10^5$, $Ha=0$ and for a 30×30 mesh. The period is $T_0 \approx 0.1$.

bifurcation from the static branch and this is a pattern that persisted throughout this numerical investigation as will be seen in the following.

In the above parameter range the nature of the periodic state that dominates the dynamics is also of interest. Focusing on the stream function we note, Fig. 12, that during one period of the motion the two major recirculation cells periodically assume a more centered position, each one occupying a major part of the left and right half of the cavity. This behavior was anticipated by the nature of the eigenvector at the bifurcation point, and leads to a more efficient cooling of the cavity, since it enhances heat transfer by engaging its hotter central part in the circulatory motion of the left and right parts of the cavity, on an alternating basis during one period. This effect is illustrated in Fig. 10 where the bifurcation diagram shown in Fig. 9 is redrawn in terms of the average cavity temperature. The dots indicate average cavity temperature that is also averaged over one period of oscillations, and is used as a means to represent the oscillatory state in the bifurcation diagram. In the small insert of Fig. 10 focusing on the bifurcation diagram after the Hopf bifurcation, the tendency of the periodic solution to lead to lower average cavity temperatures is clearly shown. In addition, the difference in the amount of heat being removed through the two vertical sides, averaged over the period $\langle Nu_L - Nu_R \rangle$, was found to decrease when compared with the steady state solution and this discrepancy was intensified as Gr increased, indicating the role of symmetry in the stability of the periodic branch and the effectiveness of heat removal. At the same time the period of the oscillations tends to increase as Gr increases, Table V(a), a tendency that is also reflected in the variation of the imaginary part of the most unstable eigenvalue of the steady state solution, which was seen to decrease as Gr increased, Table I.

As Gr further increases additional eigenvalues become unstable and soon the system response becomes chaotic. This is illustrated in Figs. 13(a) and 13(b) where the time evolution of the average cavity temperature and the transverse fluid velocity calculated at the lower left region of the cavity are depicted, along with the Fourier decomposition of the

latter. The spectrum is broadband, as expected for a chaotic response, with peaks in the frequency range provided by the eigenvalues furnished by stability analysis, see Table IV(a). Stable periodic and chaotic oscillations have been observed for similar flow configurations with the one examined here in numerical investigations available in the literature.^{14,26} The break-up of symmetry and the onset of periodic and chaotic oscillations in a volumetrically heated square cavity is examined in the first of these studies,¹⁴ whereas the stabilizing effect of the magnetic field and the destabilizing effect of internal heat generation were pointed out in the second one,²⁶ again for the case of a square cavity.

TABLE V. (a) Evolution of the period of the oscillatory motion with Gr ; $S=10^5$, $Ha=0$. The value provided for $Gr=5800$ corresponds to the imaginary part of the first unstable eigenvalue that crosses the real axis. Numerical values are obtained by performing FFT on the time series of the average cavity temperature, T_{AV} , and identifying the dominant frequency. (b) Evolution of the period of the oscillatory motion with Ha ; $S=10^5$, $Gr=10^4$. The value provided for $Ha=11$ corresponds to the imaginary part of the first unstable eigenvalue that crosses the real axis. Numerical values are obtained by performing FFT on the time series of the average cavity temperature, T_{AV} , and identifying the dominant frequency.

(a) $Ha=0$, $S=10^5$	
Gr	T_0
5 800	$0.098=2\pi/64.3$
6 000	0.098
6 500	0.102
9 400	0.112
10 000	0.113
15 500	0.122
(b) $Gr=10^4$, $S=10^5$	
Ha	T_0
11	$0.13=2\pi/47.2$
8	0.125
5	0.12
2.5	0.114
0	0.113

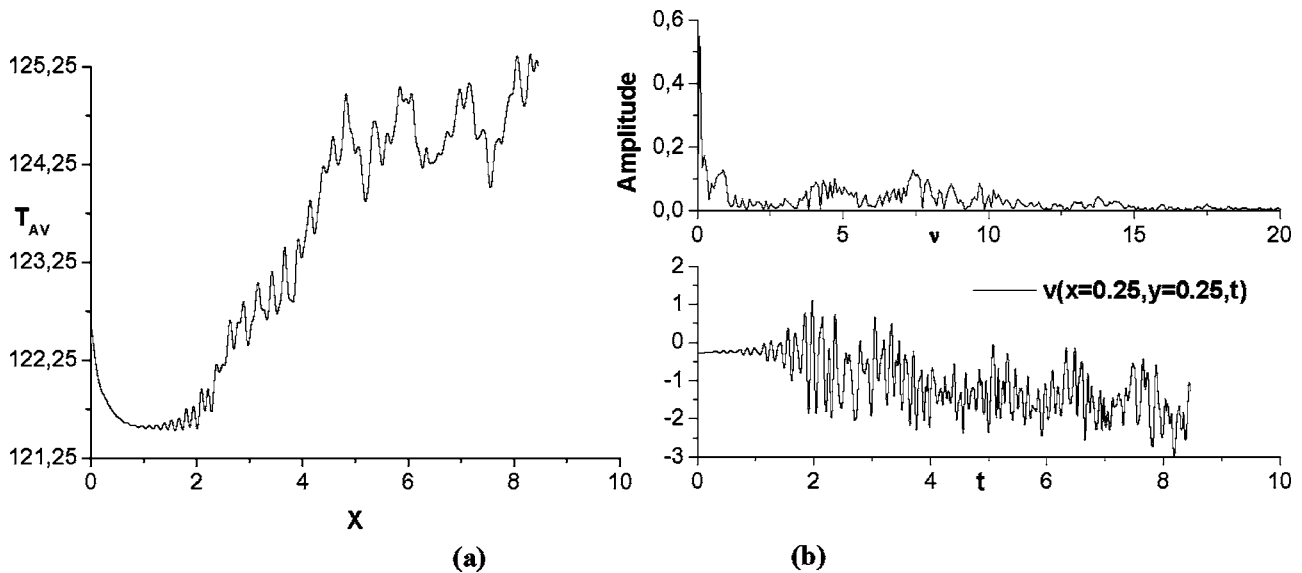


FIG. 13. (a) Dynamic evolution of the average cavity temperature T_{AV} and (b) time series and Fourier transform of the transverse velocity, $v(x=0.25, y=0.25, t)$, at the center of the lower left part of the cavity; $Ha=0$, $Gr=60\,000$, $S=10^5$ with initial condition obtained at the steady state solution for $Gr=56\,000$; $\nu=\omega/(2\pi)$ denotes the frequency of the oscillations.

The nature of the Hopf bifurcation was also examined using Ha as the operating parameter. Indeed it was seen that for high Ha values the static branch is stable and dominates the long time dynamics, whereas as Ha decreases beyond a certain critical value that depends on Gr the system exhibits an oscillatory behavior. The relevant bifurcation diagram for the case with $Gr=10^4$ and $S=10^5$ is shown in Fig. 14(a) where the oscillatory branch bifurcates supercritically to lower Ha values when $Ha \approx 11$, in which case there is a growing asymmetry in the heat being removed from the two vertical sides of the cavity, Fig. 14(b). At this value of Ha there is an exchange of stability between the two branches with the Hopf branch gaining stability. The eigenvector that corresponds to the unstable eigenvalue is very similar to the one obtained when $Ha=0$. The tendency for the bifurcating branch to lead to a lower average cavity temperature is also evident in Fig. 14(a), as well as in the time series of T_{AV} in Fig. 15. The reason for the improved heat removal can be associated to the motion of the fluid in the cavity as predicted for the oscillatory solution. In the oscillatory solution the two recirculation vortices engage a larger portion of the cavity fluid, in comparison to the steady state solution, as a result of the smaller cell that is periodically attached to and removed from the major cell on the right-hand side of the cavity. The streamline pattern when $Ha=12$ is more symmetric than both the steady state and oscillatory solutions obtained when $Ha=5$; nevertheless it is not very useful as far as heat removal is concerned because it does not provide sufficient mixing of the fluid in the cavity. The period of the oscillatory motion tends to decrease from the value predicted by stability analysis as Ha decreases, see Table V(b). This effect was also observed in the evolution of the imaginary part of the most unstable eigenvalue with varying Ha , Table II.

The supercritical nature of the Hopf bifurcation was verified for the entire parameter range that was examined in the present study. The only difference with increasing Ha

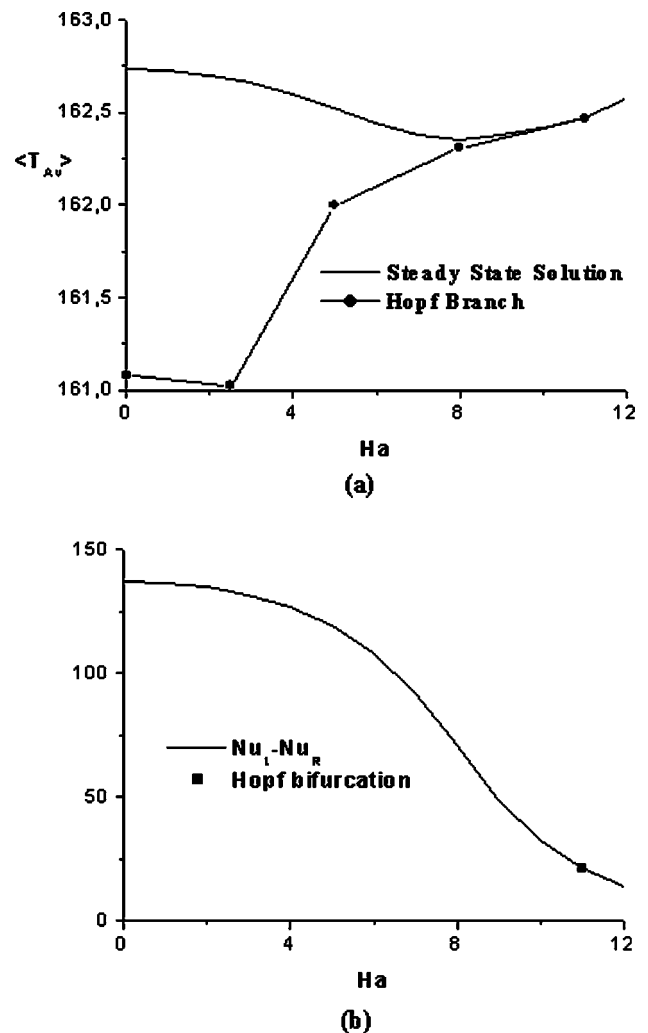


FIG. 14. Bifurcation diagram of the steady state and Hopf branches in terms of the (a) average cavity temperature, $\langle T_{AV} \rangle$ and (b) ΔNu , as a function of Ha ; $S=10^5$, $Gr=10^4$.

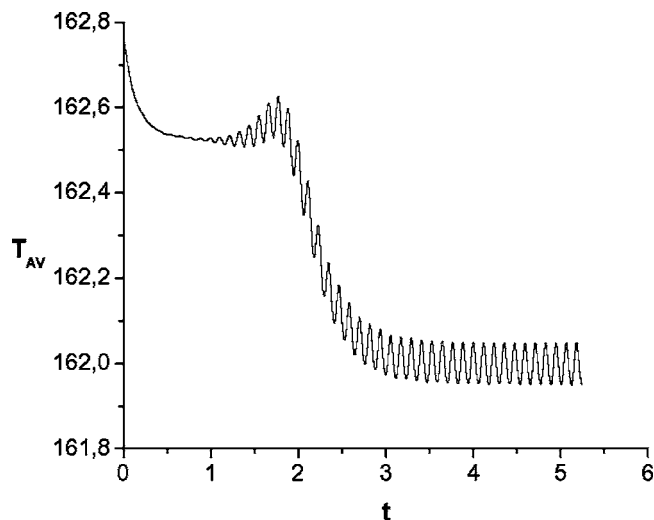


FIG. 15. Dynamic evolution of the average cavity temperature T_{AV} when $Ha=5$, $S=10^5$, and $Gr=10^4$ with initial condition at the steady state solution for $Gr=9\,900$.

was the evolution of the relevant eigenvector that gradually became more symmetric as Ha increased, $12.5 \leq Ha \leq 20$, with additional smaller recirculation cells, and the switch in the order of the first two eigenmodes that cross the real axis in the interval $15 \leq Ha \leq 20$. The case for $Ha=12.5$ with $Gr=55\,000$ and $S=10^5$, was simulated numerically with a 30×30 mesh. For this Ha value the structure of the most unstable eigenvectors is very similar to that obtained in the range of large Ha , while a 30×30 mesh is sufficient to capture the system dynamics. The time variation and Fourier transform of the transverse fluid velocity at the center of the lower left region of the cavity, $v(x=0.25, y=0.25, t)$, along with a sequence of the streamline pattern obtained at various instances of the steady oscillatory motion, are depicted in Figs. 16(b) and 17. The supercritical nature of the periodic branch is evident, as well as the dominant time scales which are also seen to agree with those predicted by linear stability. For the above parameter values eigenvalue calculations with a 30×30 and 60×60 mesh provide two unstable eigenvalues, $\sigma_1=0.36 \pm 26i$ and $\sigma_2=0.0150 \pm 53.8i$. Indeed, the Fourier decomposition of the time series reveals a dominant peak at frequency $\nu \approx 4.05$ and two smaller peaks corresponding to the second harmonic of the dominant eigenvalue at $\nu \approx 8.1$ and to the second unstable eigenvalue at $\nu \approx 8.5$. The final periodic state of the system is determined by the most unstable eigenvalue with a period of $T_0 \approx 0.25$, while the streamline structure of the periodic solution exhibits smaller internal recirculation cells that periodically grow inside the two major cells, Figs. 17(b)–17(f). The left and right-hand sides of the cavity exhibit such structures with a phase difference of π within one period of the oscillations, and this is reflected in the temperature contours as well. The streamline structure of the steady state solution for $Gr=55\,000$ is shown in Fig. 17(a). Finally the evolution of the average cavity temperature, shown in Fig. 16(a), exhibits a very interesting behavior that is characteristic of the high Ha regime. After a long transient it settles to a value that is actually larger than the one corresponding to the steady state solution, a distinct

difference with the system behavior that was discussed above for smaller Ha values. This behavior is correlated to the change in the bifurcation diagram when $Ha \geq 12.5$ and identifies the existence of an upper threshold in Ha if proper cooling of the cavity is of interest.

For larger Ha values a 60×60 mesh is necessary for proper description of the dynamics, thus rendering the corresponding simulations very time consuming. The cases for $Ha=15$ with $Gr=74\,000$ and $Ha=20$ with $Gr=135\,000$, $S=10^5$, were simulated with a 60×60 mesh until the early stages of the onset of periodic motion, and the numerically obtained dynamic behavior supports the supercritical structure of the bifurcation and recovers the appropriate time scales.

VII. CONCLUSIONS

The stability of steady state solutions for a differentially heated square cavity in the presence of a horizontal magnetic field and a uniform heat source was examined in the context of two-dimensional disturbances. Extensive eigenvalue calculations followed by dynamic simulations revealed that, provided there is nonvanishing heat generation inside the cavity, the system undergoes a supercritical Hopf bifurcation leading to a periodic branch. The bifurcation occurs when the asymmetry in the heat being removed through the two vertical sides of the cavity becomes large enough and leads to a solution that is characterized by a more symmetric configuration of the two major recirculating cells that determine the efficiency of heat transfer in the cavity and a lower average cavity temperature. The asymmetry is intensified by increasing Gr which measures the effect of buoyancy in the flow. Beyond a certain critical value, Gr_{cr} , steady solutions are unstable and periodicity sets in. Further increase of Gr produces additional unstable eigenvalues and renders the response of the system chaotic. Heat production, raising S , destabilizes the system whereas application of a magnetic field, raising Ha , stabilizes it in terms of increasing and decreasing Gr_{cr} , respectively. The Hopf bifurcation was seen to be supercritical for the entire range of Ha that was investigated, $0 \leq Ha \leq 20$. Raising Ha beyond a certain value, Ha is roughly 12 when $S=10^5$, mainly renders the bifurcating periodic branch more symmetric and decreases the frequency of oscillations until a minimum occurs in the range $15 \leq Ha \leq 20$ and the frequency starts increasing again. The latter effect is a result of a different eigenmode crossing the real axis. In addition, when $Ha \geq 12.5$ the structure of the bifurcation diagram ΔNu vs Gr changes and the second maximum in ΔNu disappears. This results in a more symmetric eigenvector with additional smaller recirculation cells and identifies a range in Ha over which the periodic solution leads to a higher average cavity temperature. Consequently, there is an upper threshold of the magnetic field intensity, characterized by Ha , for efficient heat removal at large Gr .

In a similar flow configuration but, in the absence of heat production, with the magnetic field assuming various angles with respect to gravity and with the aspect ratio A set to 0.5,²⁷ the case of two recirculating rolls was seen to produce a supercritical Hopf bifurcation in the (Gr, Ha) parameter

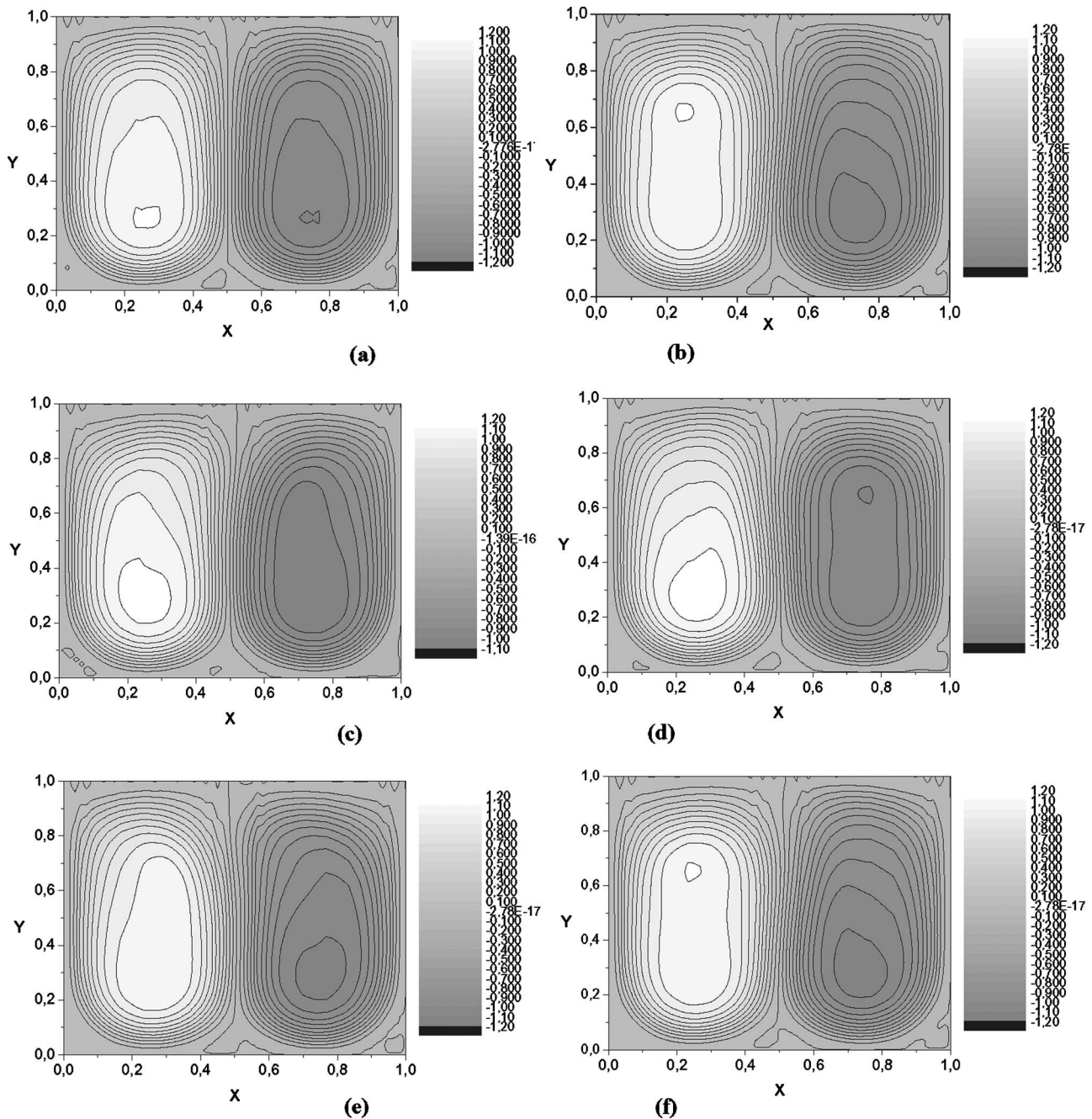


FIG. 17. Streamline pattern corresponding (a) to the steady state solution, and (b)–(f) obtained within one period of the steady oscillatory motion; $Ha=12.5$, $Gr=55\,000$, and $S=10^5$. The initial condition was obtained at the steady state solution for $Gr=50\,000$ and the period of the steady oscillation is $T_0 \approx 0.25$.

space only in the range of small Ha values, $Ha < 8$, when the magnetic field is horizontal. For large Ha values the bifurcation is subcritical, eventually leading to a single cell pattern. In essence, two cell patterns were not seen to persist for large Ha values, $Ha > 12$, contrary to single cell structures that were obtained for large Ha . This discrepancy was attributed partly to the effect of the Hartmann and side layers developing in the vicinity of the cavity boundaries as Ha increases. In the present study two cell structures were seen to persist for large Ha values and bifurcate to an oscillatory state for large enough $Gr=Gr_{cr}$. The destabilizing effect of the Ha and side layers was not seen to affect this dynamic pattern, prob-

ably because Gr_{cr} increases significantly as Ha increases in which case the ratio $Gr_{cr}^{1/2}/Ha^2$ does not become small enough to determine the system behavior.

As a next step the stability of the system subject to three-dimensional disturbances will be investigated in order to identify the effect of Hartmann braking on the two-cell structure that was seen to persist in the parameter range that was examined here. It was seen elsewhere¹² that the Lorenz force tends to eliminate vortices that are arranged perpendicularly to the magnetic field and, for a long duct with a cross-sectional aspect ratio of 10, to produce quasi-two-dimensional vortices that are aligned with the magnetic field.

Conducting a two-dimensional stability analysis, employing the methodology described in Secs. III and IV, on the base state of pure heat conduction that was utilized in Ref. 12 and for the same parameter range, it was seen that a bifurcation to a steady state solution characterized by a number of recirculation cells occurs when $Gr \approx 3 \times 10^6$ when $Ha=100$, $A=10$, and $Pr=0.02$. However, it was shown in the above study that three-dimensional instabilities leading to an arrangement of the vortices that is aligned to the magnetic field arise at a much lower value of Gr for the same parameter range. It will be of interest to examine the extent to which the steady state or periodic solutions that were observed here, can be anticipated by three-dimensional instabilities that will destroy the existing two-cell structure and lead to a different arrangement that is aligned to the magnetic field.

ACKNOWLEDGMENTS

The author wishes to acknowledge Dr. Theophanes Grammenos for fruitful discussions on the basic principles of electromagnetism and Mr. Nikos Tsapralis for performing steady state calculations in his diploma thesis. This work was performed in the framework of the EURATOM-Hellenic Republic Association and is supported by the European Union within the Fusion Program. The content of this publication is the sole responsibility of the author and it does not necessarily represent the views of the Commission or its services.

- ¹Gary A. Glatzmaier and Paul H. Roberts, "A three-dimensional self-consistent computer simulation of a geomagnetic field reversal," *Nature* (London) **377**, 203 (1995).
- ²A. Kharicha, S. Molokov, S. Aleksandrova, and L. Bühler, "Buoyant convection in the helium-cooled lithium lead blanket, in a strong uniform magnetic field," FZKA 6959, Forschungszentrum Karlsruhe (2004).
- ³R. Brown, "Theory of transport processes in single crystal growth from the melt," *AICHE J.* **34**, 881 (1988).
- ⁴N. A. Pelekasis, C. Economou, and J. A. Tsamopoulos, "Linear oscillations and stability of a liquid bridge in a dc electric field," *Phys. Fluids* **13**, 3564 (2001).
- ⁵L. Bühler, "Laminar buoyant magnetohydrodynamic flow in vertical rectangular ducts," *Phys. Fluids* **10**, 223 (1998).
- ⁶R. C. Reed and B. F. Picologlou, "Sidewall flow instabilities in liquid-metal MHD flow under blanket relevant conditions," *Fusion Technol.* **15**, 705 (1989).
- ⁷A. L. Ting, J. S. Walker, T. J. Moon, C. B. Reed, and B. F. Picologlou, "Linear stability analysis for high velocity boundary layers in liquid metal magnetohydrodynamic flows," *Int. J. Eng. Sci.* **29**, 939 (1991).
- ⁸U. Burr, L. Barleon, U. Müller, and A. Tsinober, "Turbulent transport of

- momentum and heat in magnetohydrodynamic rectangular duct flow with strong sidewall jets," *J. Fluid Mech.* **406**, 247 (2000).
- ⁹R. J. Lingwood and T. Alboussière, "On the stability of the Hartmann layer," *Phys. Fluids* **11**, 2058 (1999).
- ¹⁰P. Moresco and T. Alboussière, "Weakly nonlinear stability of Hartmann boundary layers," *Eur. J. Mech. B/Fluids* **22**, 345 (2003).
- ¹¹L. Bühler, "Laminar buoyant magnetohydrodynamic flow in vertical rectangular ducts," *Phys. Fluids* **10**, 223 (1998).
- ¹²U. Burr and U. Müller, "Rayleigh-Bernard convection in liquid metal layers under the influence of a horizontal magnetic field," *J. Fluid Mech.* **453**, 345, (2002).
- ¹³M. Takashima, "The stability of natural convection in a vertical layer of electrically conducting fluid in the presence of a transverse magnetic field," *Fluid Dyn. Res.* **14**, 121 (1994).
- ¹⁴S. Arcidiacono, I. Di Piazza, and M. Ciofalo, "Low-Prandtl number natural convection in volumetrically heated rectangular enclosures. II. Square cavity, $AR=1$," *Int. J. Heat Mass Transfer* **44**, 537 (2001).
- ¹⁵M. Ciofalo and F. Cricchio, "Influence of a magnetic field on liquid metal free convection in an internally heated cubic enclosure," *Int. J. Numer. Methods Heat Fluid Flow* **12**, 687 (2002).
- ¹⁶J. P. Garandet, T. Alboussière, and R. Moreau, "Buoyancy driven convection in a rectangular enclosure with a transverse magnetic field," *Int. J. Heat Mass Transfer* **35**, 741 (1992).
- ¹⁷R. B. Lehoucq and J. A. Scott, "An evaluation of software for computing eigenvalues of sparse nonsymmetric matrixes," MCS-P547-1195, Argonne National Laboratory (1996).
- ¹⁸G. Iooss and D. D. Joseph, *Elementary Stability and Bifurcation Theory*, Undergraduate Texts in Mathematics (Springer-Verlag, New York, 1980).
- ¹⁹R. Seydel, *From Equilibrium to Chaos: Practical Bifurcation and Stability Analysis* (Elsevier, New York, 1988).
- ²⁰P. M. Gresho and R. L. Sani, *Incompressible Flow and the Finite Element Method* (Wiley, New York, 1998).
- ²¹E. A. Burroughs, L. A. Romero, R. B. Lehoucq, and A. G. Salinger, "Linear stability of flow in a differentially heated cavity via large-scale eigenvalue calculations," *Int. J. Numer. Methods Heat Fluid Flow* **14**, 803 (2004).
- ²²J. P. Garandet, T. Alboussière, and R. Moreau, "Buoyancy driven convection in a rectangular enclosure with a transverse magnetic field," *Int. J. Heat Mass Transfer* **35**, 741 (1992).
- ²³B. Schulz, "Thermophysical properties of the Li(17) Pb(83) alloy," *Fusion Eng. Des.* **14**, 199 (1991).
- ²⁴H. Ben Hadid, D. Henry, and S. Kaddeche, "Numerical study of convection in the horizontal Bridgeman configuration under the action of a constant magnetic field. Part I. Two-dimensional flow," *J. Fluid Mech.* **333**, 23 (1977).
- ²⁵T. Alboussière, J. P. Garandet, and R. Moreau, "Asymptotic analysis and symmetry in MHD convection," *Phys. Fluids* **8**, 2215 (1996).
- ²⁶I. E. Sarris, S. C. Kakarantzas, A. P. Grecos, and N. S. Vlachos, "MHD natural convection in a laterally and volumetrically heated square cavity," *Int. J. Heat Mass Transfer* **48**, 3443 (2005).
- ²⁷A. Yu. Gelfgat and P. Z. Bar-Yoseph, "The effect of an external magnetic field on oscillatory instability of convective flows in a rectangular cavity," *Phys. Fluids* **13**, 2269 (2001).